

## Precision electromagnetic structure of decuplet baryons in the chiral regime

S. Boinepalli,<sup>1</sup> D.B. Leinweber,<sup>1</sup> P.J. Moran,<sup>1</sup> A.G. Williams,<sup>1</sup> J.M. Zanotti,<sup>2</sup> and J.B. Zhang<sup>3</sup><sup>1</sup>*Department of Physics and Mathematical Physics and  
Special Research Centre for the Subatomic Structure of Matter,  
University of Adelaide, 5005, Australia*<sup>2</sup>*School of Physics & Astronomy, University of Edinburgh, Edinburgh EH9 3JZ, UK*<sup>3</sup>*Department of Physics, Zhejiang University, Hangzhou, Zhejiang 310027, P.R. China*

The electromagnetic properties of the baryon decuplet are calculated in quenched QCD on a  $20^3 \times 40$  lattice with a lattice spacing of 0.128 fm using the fat-link irrelevant clover (FLIC) fermion action with quark masses providing a pion mass as low as 300 MeV. Magnetic moments and charge radii are extracted from the electric and magnetic form factors for each individual quark sector. From these, the corresponding baryon properties are constructed. We present results for the higher order moments of the spin-3/2 baryons, including the electric quadrupole moment  $E2$  and the magnetic octupole moment  $M3$ . The world's first determination of a non-zero  $M3$  form factor for the  $\Delta$  baryon is presented. With these results we provide a conclusive analysis which shows that decuplet baryons are deformed. We compare the decuplet baryon results from a similar lattice calculation of the octet baryons. We establish that the environment sensitivity is far less pronounced in the case of the decuplet baryons compared to that in the octet baryons. A surprising result is that the charge radii of the decuplet baryons are generally smaller than that of the octet baryons. The magnetic moment of the  $\Delta^+$  reveals a turn over in the low quark mass region, making it smaller than the proton magnetic moment. These results are consistent with the expectations of quenched chiral perturbation theory. A similar turn over is also noticed in the magnetic moment of the  $\Sigma^{*0}$ , but not for  $\Xi^*$  where only kaon loops can appear in quenched QCD. The electric quadrupole moment of the  $\Omega^-$  baryon is positive when the negative charge factor is included, and is equal to  $0.86 \pm 0.12 \times 10^{-2} \text{ fm}^2$ , indicating an oblate shape.

PACS numbers: 12.39.Fe, 12.38.Gc, 13.40.Em, 14.20.Dh, 14.20.Jn

## I. INTRODUCTION

The study of the electromagnetic properties of baryons provides valuable insight into the non-perturbative structure of QCD (see Refs. [1, 2, 3, 4, 5] for recent reviews). Baryon charge radii and magnetic moments provide an excellent opportunity to observe the non-analytic behavior predicted by chiral effective field theory ( $\chi$ EFT). Since these are inherently non-perturbative properties of hadrons, first-principles calculations on the lattice are essential for our understanding of hadronic structure, and indeed there has been much progress in this direction, mainly for the nucleon and pseudoscalar states (see [6] for a review). For decuplet baryons, however, there has been very little progress since Ref. [7] which appeared almost 15 years ago. However, renewed interest appeared recently [8, 9].

The Adelaide group has been investigating the electromagnetic structure of hadrons for several years now. In Refs. [10, 11], we presented a novel method for determining the strange quark contribution to the nucleon's electromagnetic form factors, the results of which were later confirmed by an improved analysis of old experimental data [12] and new data from parity violating experiments at JLab [13]. This was followed by an in-depth study in quenched QCD of the electromagnetic properties of the octet baryons [14]. Of particular interest was an observed environmental isospin dependence of the strange quark distributions in  $\Lambda^0$  and  $\Sigma^0$ . More recently, we performed an investigation into the pseudoscalar and vector meson

electromagnetic form factors [15]. Here we determined that the  $\rho^+$  meson has a negative quadrupole moment, indicating that the  $\rho$  meson is oblate.

In this paper we continue our study of the electromagnetic structure of hadrons and present a quenched lattice QCD calculation of the electromagnetic form factors of  $SU(3)_{\text{flavor}}$  decuplet baryons. From these form factors we determine magnetic moments, charge and magnetic radii and present results for the electric quadrupole and magnetic octupole moments.

On the lattice, decuplet baryons are stable as a result of the unphysical large quark masses that are used in present calculations and the finite volume of the lattice. Decay to a pion and an octet baryon is forbidden by energy conservation. However, stability of decuplet baryons is common to most hadronic models. In this sense, lattice results provide a useful forum in which the strengths and weaknesses of various models may be identified. The lattice results also provide access to observables not readily available with present experiments such as the higher-order multipole moments of the  $\Omega^-$  which is stable to strong interactions.

An examination of decuplet baryon structure in lattice QCD enables one to study new aspects of non-perturbative quark-gluon dynamics. In analyzing the results we make comparisons within the baryon decuplet and with the octet results [14] which provide insights into the spin dependence of quark interactions.

The  $E2$  and  $M3$  moments accessible in spin-3/2 systems provide insights into the shape of the decuplet

baryon ground state. These higher-order moments also have the potential to discriminate between various model descriptions of hadronic phenomena.

To put our results into perspective, we compare our calculations with experimental measurements where available, and with the predictions of Quenched Chiral Perturbation Theory (QχPT).

The decuplet baryon interpolating fields used in the correlation functions are discussed in Sec. II A. The extraction of baryon mass and electromagnetic form factors proceeds through a calculation of two and three-point correlation functions. These are discussed in Sec. II B. The two and three point functions for decuplet baryons are discussed in Secs. II C and II D. Throughout this analysis we employ the lattice techniques introduced in [7], and these are summarized in Sec. III. In Sec. IV we outline the methods used in our analysis of the lattice two and three point functions. Our results are presented and discussed in Sec. V, and summarized in Sec. VI.

## II. THEORETICAL FORMALISM

### A. Interpolating Fields

The commonly used interpolating field for exciting the  $\Delta^{++}$  resonance from the QCD vacuum takes the long established [16, 17] form of

$$\chi_\mu^{\Delta^{++}}(x) = \epsilon^{abc} (u^{Ta}(x) C \gamma_\mu u^b(x)) u^c(x). \quad (2.1)$$

Unless otherwise noted, we follow the notation of Sakurai [18]. The Dirac gamma matrices are Hermitian and satisfy  $\{\gamma_\mu, \gamma_\nu\} = 2\delta_{\mu\nu}$ , with  $\sigma_{\mu\nu} = \frac{1}{2i}[\gamma_\mu, \gamma_\nu]$ .  $C = \gamma_4\gamma_2$  is the charge conjugation matrix,  $a, b, c$  are color indices,  $u(x)$  is a  $u$ -quark field, and the superscript  $T$  denotes transpose. The generalization of this interpolating field

for the  $\Delta^+$  composed of two  $u$  quarks and one  $d$  quark has the form

$$\chi_\mu^{\Delta^+}(x) = \frac{1}{\sqrt{3}} \epsilon^{abc} \left[ 2 (u^{Ta}(x) C \gamma_\mu d^b(x)) u^c(x) + (u^{Ta}(x) C \gamma_\mu u^b(x)) d^c(x) \right]. \quad (2.2)$$

Other decuplet baryon interpolating fields are obtained with the appropriate substitutions of  $u(x)$ ,  $d(x) \rightarrow u(x)$ ,  $d(x)$  or  $s(x)$ . The interpolating field for  $\Sigma^{*0}$  is given by the symmetric generalization

$$\chi_\mu^{\Sigma^{*0}}(x) = \sqrt{\frac{2}{3}} \epsilon^{abc} \left[ (u^{Ta}(x) C \gamma_\mu d^b(x)) s^c(x) + (d^{Ta}(x) C \gamma_\mu s^b(x)) u^c(x) + (s^{Ta}(x) C \gamma_\mu u^b(x)) d^c(x) \right]. \quad (2.3)$$

The  $SU(2)$ -isospin symmetry relationship for  $\Sigma^*$  form factors

$$\Sigma^{*0} = \frac{\Sigma^{*+} + \Sigma^{*-}}{2}, \quad (2.4)$$

may be easily seen in the  $\Sigma^{*0}$  interpolating field by noting

$$\epsilon^{abc} (s^{Ta}(x) C \gamma_\mu u^b(x)) d^c(x) = \epsilon^{abc} (u^{Ta}(x) C \gamma_\mu s^b(x)) d^c(x). \quad (2.5)$$

### B. Correlation functions

Two-point correlation functions at the quark level are obtained through the standard procedure of contracting pairs of quark fields. Considering the  $\Delta^+$  correlation function at the quark level and performing all possible quark field contractions gives the two-point function as

$$\begin{aligned} \left\langle T \left( \chi_\mu^{\Delta^+}(x) \bar{\chi}_\nu^{\Delta^+}(0) \right) \right\rangle &= \frac{1}{3} \epsilon^{abc} \epsilon^{a'b'c'} \left\{ 4S_u^{aa'} \gamma_\nu C S_u^{Tbb'} C \gamma_\mu S_d^{cc'} + 4S_u^{aa'} \gamma_\nu C S_d^{Tbb'} C \gamma_\mu S_u^{cc'} \right. \\ &\quad + 4S_d^{aa'} \gamma_\nu C S_u^{Tbb'} C \gamma_\mu S_u^{cc'} + 2S_u^{aa'} \text{tr} \left[ \gamma_\nu C S_u^{Tbb'} C \gamma_\mu S_d^{cc'} \right] \\ &\quad \left. + 2S_u^{aa'} \text{tr} \left[ \gamma_\nu C S_d^{Tbb'} C \gamma_\mu S_u^{cc'} \right] + 2S_d^{aa'} \text{tr} \left[ \gamma_\nu C S_u^{Tbb'} C \gamma_\mu S_u^{cc'} \right] \right\} \end{aligned} \quad (2.6)$$

where the quark-propagator  $S_u^{aa'} = T \left( u^a(x) \bar{u}^{a'}(0) \right)$  and similarly for other quark flavors.  $SU(3)_{\text{flavor}}$  symmetry is clearly displayed in this equation.

In determining the three point function, one encounters two topologically different ways of performing the current insertion. Figure 1 displays skeleton diagrams for these two insertions. These diagrams may be dressed with an arbitrary number of gluons. Diagram (a) illus-

trates the connected insertion of the current to one of the valence quarks of the baryon. Diagram (b) accounts for the alternative time ordering where the current first produces a disconnected  $q\bar{q}$  pair which in turn interacts with the valence quarks of the baryon via gluons.

The number of terms in the three-point function is four times that in Eq. (2.6). The correlation function relevant for a  $\Delta^+$  three-point function is

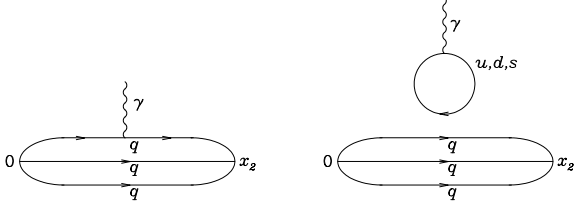


FIG. 1: Diagrams illustrating the two topologically different insertions of the current within the framework of lattice QCD.

$$\begin{aligned}
T\left(\chi_\mu^{\Delta^+}(x_2) j^\alpha(x_1) \bar{\chi}_\nu^{\Delta^+}(0)\right) &= \frac{1}{3} \epsilon^{abc} \epsilon^{a'b'c'} \left\{ \right. \\
&4\widehat{S}_u^{aa'} \gamma_\nu C S_u^{Tbb'} C \gamma_\mu S_d^{cc'} + 4\widehat{S}_u^{aa'} \gamma_\nu C S_d^{Tbb'} C \gamma_\mu S_u^{cc'} + 4\widehat{S}_d^{aa'} \gamma_\nu C S_u^{Tbb'} C \gamma_\mu S_u^{cc'} \\
&+ 4S_u^{aa'} \gamma_\nu C \widehat{S}_u^{Tbb'} C \gamma_\mu S_d^{cc'} + 4S_d^{aa'} \gamma_\nu C \widehat{S}_u^{Tbb'} C \gamma_\mu S_u^{cc'} + 4S_u^{aa'} \gamma_\nu C \widehat{S}_d^{Tbb'} C \gamma_\mu S_u^{cc'} \\
&+ 4S_u^{aa'} \gamma_\nu C S_d^{Tbb'} C \gamma_\mu \widehat{S}_u^{cc'} + 4S_d^{aa'} \gamma_\nu C S_u^{Tbb'} C \gamma_\mu \widehat{S}_u^{cc'} + 4S_u^{aa'} \gamma_\nu C S_u^{Tbb'} C \gamma_\mu \widehat{S}_d^{cc'} \\
&+ 2\widehat{S}_u^{aa'} \text{tr} \left[ \gamma_\nu C S_u^{Tbb'} C \gamma_\mu S_d^{cc'} \right] + 2\widehat{S}_u^{aa'} \text{tr} \left[ \gamma_\nu C S_d^{Tbb'} C \gamma_\mu S_u^{cc'} \right] + 2\widehat{S}_d^{aa'} \text{tr} \left[ \gamma_\nu C S_u^{Tbb'} C \gamma_\mu S_u^{cc'} \right] \\
&+ 2S_u^{aa'} \text{tr} \left[ \gamma_\nu C \widehat{S}_u^{Tbb'} C \gamma_\mu S_d^{cc'} \right] + 2S_d^{aa'} \text{tr} \left[ \gamma_\nu C \widehat{S}_u^{Tbb'} C \gamma_\mu S_u^{cc'} \right] + 2S_u^{aa'} \text{tr} \left[ \gamma_\nu C \widehat{S}_d^{Tbb'} C \gamma_\mu S_u^{cc'} \right] \\
&+ 2S_u^{aa'} \text{tr} \left[ \gamma_\nu C S_d^{Tbb'} C \gamma_\mu \widehat{S}_u^{cc'} \right] + 2S_d^{aa'} \text{tr} \left[ \gamma_\nu C S_u^{Tbb'} C \gamma_\mu \widehat{S}_u^{cc'} \right] + 2S_u^{aa'} \text{tr} \left[ \gamma_\nu C S_u^{Tbb'} C \gamma_\mu \widehat{S}_d^{cc'} \right] \left. \right\} \\
&+ \sum_{q=u,d,s} e_q \sum_i \text{tr} \left[ S_q^{ii}(x_1, x_1) \gamma_\mu \right] \frac{1}{3} \epsilon^{abc} \epsilon^{a'b'c'} \left\{ \right. \\
&4S_u^{aa'} \gamma_\nu C S_u^{Tbb'} C \gamma_\mu S_d^{cc'} + 4S_u^{aa'} \gamma_\nu C S_d^{Tbb'} C \gamma_\mu S_u^{cc'} + 4S_d^{aa'} \gamma_\nu C S_u^{Tbb'} C \gamma_\mu v S_u^{cc'} \\
&+ 2S_u^{aa'} \text{tr} \left[ \gamma_\nu C S_u^{Tbb'} C \gamma_\mu S_d^{cc'} \right] + 2S_u^{aa'} \text{tr} \left[ \gamma_\nu C S_d^{Tbb'} C \gamma_\mu S_u^{cc'} \right] + 2S_d^{aa'} \text{tr} \left[ \gamma_\nu C S_u^{Tbb'} C \gamma_\mu S_u^{cc'} \right] \left. \right\}
\end{aligned} \tag{2.7}$$

where

$$\widehat{S}_q^{aa'}(x_2, x_1, 0) = e_q \sum_i S_q^{ai}(x_2, x_1) \gamma_\alpha S_q^{ia'}(x_1, 0), \tag{2.8}$$

denotes the connected insertion of the probing current to a quark of charge  $e_q$ . Here we have explicitly selected the electromagnetic current. However, the present discussion may be generalized to any quark-field-based current operator bilinear in the quark fields.

The latter term of Eq. (2.7) accounts for the disconnected quark loop contribution depicted in Fig. 1b. The sum over the quarks running around the loop has been restricted to the flavors relevant to the ground state baryon octet and decuplet. In the  $SU(3)_{\text{flavor}}$  limit the sum vanishes for the electromagnetic current. However, the heavier strange quark mass allows for a nontrivial result. Due to the technical difficulties of numerically estimating  $M^{-1}$  for the squared lattice volume of diagonal spatial indices, these contributions have been omitted from lat-

tice QCD calculations of electromagnetic structure in the spirit of Q $\chi$ PT, and we will also do so here. For other observables such as the scalar density or forward matrix elements of the axial vector current relevant to the spin of the baryon, the “charges” running around the loop do not sum to zero. In this case the second term of Eq. (2.7) can be just as significant as the connected term [19, 20].

An examination of Eq. (2.7) reveals complete symmetry among the quark flavors in the correlation function. For example, wherever a  $d$  quark appears in the correlator, a  $u$  quark also appears in the same position in another term. An interesting consequence of this is that the connected insertion of the electromagnetic current for  $\Delta^0$  vanishes. All electromagnetic properties of the  $\Delta^0$  have their origin strictly in the disconnected loop contri-

bution. Physically, what this means is that the valence wave function for each of the quarks in the  $\Delta$  resonances are identical under charge symmetry.

### C. Two-point Green functions

In this and the following subsection discussing correlation functions at the hadronic level, the Dirac representation of the  $\gamma$ -matrices is used to facilitate calculations of the  $\gamma$ -matrix algebra. It is then a simple task to account for the differences in  $\gamma$ -matrix and metric definitions in reporting the final results using Sakurai's notation.

The extraction of baryon mass and electromagnetic form factors proceeds through the calculation of the ensemble average (denoted  $\langle \dots \rangle$ ) of two and three-point Green functions. The two-point function for decuplet baryons is defined as

$$\langle G_{\sigma\tau}^{BB}(t; \vec{p}; \Gamma) \rangle = \sum_{\vec{x}} e^{-i\vec{p}\cdot\vec{x}} \Gamma^{\beta\alpha} \langle \Omega | T(\chi_{\sigma}^{\alpha}(x) \bar{\chi}_{\tau}^{\beta}(0)) | \Omega \rangle. \quad (2.9)$$

Here  $\Omega$  represents the QCD vacuum,  $\Gamma$  is a  $4 \times 4$  matrix in Dirac space and  $\alpha, \beta$  are Dirac indices. The subscripts  $\sigma, \tau$  are the Lorentz indices of the spin-3/2 interpolating fields. At the hadronic level one proceeds by inserting a complete set of states  $|B, p, s\rangle$  and defining

$$\langle \Omega | \chi_{\sigma}(0) | B, p, s \rangle = Z_B(p) \sqrt{\frac{M}{E_p}} u_{\sigma}(p, s), \quad (2.10)$$

where  $Z_B$  represents the coupling strength of  $\chi_{\sigma}(0)$  to the baryon  $B$ . Our use of smeared interpolators makes this momentum dependent. Momentum is denoted by  $p$ , spin by  $s$ , and  $u_{\sigma}(p, s)$  is a spin-vector in the Rarita-Schwinger formalism.  $E_p = \sqrt{\vec{p}^2 + M^2}$  and Dirac indices have been suppressed. Using the Rarita-Schwinger spin sum,

$$\sum_s u_{\sigma}(p, s) \bar{u}_{\tau}(p, s) = -\frac{\gamma \cdot p + M}{2M} \left\{ g_{\sigma\tau} - \frac{1}{3} \gamma_{\sigma} \gamma_{\tau} - \frac{2p_{\sigma} p_{\tau}}{3M^2} + \frac{p_{\sigma} \gamma_{\tau} - p_{\tau} \gamma_{\sigma}}{3M} \right\}, \quad (2.11)$$

$$\equiv \Lambda_{\sigma\tau},$$

our usual definitions for  $\Gamma$ ,

$$\Gamma_j = \frac{1}{2} \begin{pmatrix} \sigma_j & 0 \\ 0 & 0 \end{pmatrix} \quad ; \quad \Gamma_4 = \frac{1}{2} \begin{pmatrix} I & 0 \\ 0 & 0 \end{pmatrix}, \quad (2.12)$$

and  $\vec{p} = (p, 0, 0)$ , the large Euclidean time limit of the two point function takes the form

$$\langle G_{\sigma\tau}^{BB}(t; \vec{p}; \Gamma_4) \rangle = Z_B(p) \bar{Z}_B(p) \frac{M}{E_p} e^{-E_p t} \text{tr}[\Gamma_4 \Lambda_{\sigma\tau}], \quad (2.13)$$

where

$$\langle G_{00}^{BB}(t; \vec{p}; \Gamma_4) \rangle = Z_B(p) \bar{Z}_B(p) \frac{2}{3} \frac{|\vec{p}|^2}{M_B^2} \left( \frac{E_p + M_B}{2E_p} \right) e^{-E_p t}, \quad (2.14)$$

$$\langle G_{11}^{BB}(t; \vec{p}; \Gamma_4) \rangle = Z_B(p) \bar{Z}_B(p) \frac{2}{3} \frac{E_p^2}{M_B^2} \left( \frac{E_p + M_B}{2E_p} \right) e^{-E_p t}, \quad (2.15)$$

$$\langle G_{22}^{BB}(t; \vec{p}; \Gamma_4) \rangle = Z_B(p) \bar{Z}_B(p) \frac{2}{3} \left( \frac{E_p + M_B}{2E_p} \right) e^{-E_p t}, \quad (2.16)$$

$$\langle G_{33}^{BB}(t; \vec{p}; \Gamma_4) \rangle = Z_B(p) \bar{Z}_B(p) \frac{2}{3} \left( \frac{E_p + M_B}{2E_p} \right) e^{-E_p t}. \quad (2.17)$$

Here  $\bar{Z}_B(p)$  denotes the overlap associated with our smeared source.  $Z_B(p)$  is associated with the sink which need not have the same smearing.

Equations (2.14) through (2.17) provide four correla-

tion functions from which a baryon mass may be extracted. All baryon masses extracted from the different selections of Lorentz indices agree within statistical uncertainties. The combination providing the smallest sta-

tistical fluctuations is  $\langle G_{22}^{BB}(t; \vec{p}, \Gamma_4) + G_{33}^{BB}(t; \vec{p}, \Gamma_4) \rangle$  and these results are presented in section V.

It should be noted that the spin-3/2 interpolating field also has overlap with spin-1/2 baryons. For the  $\Delta$  baryons and  $\Omega^-$  this poses no problem as these baryons are the lowest lying baryons in the mass spectrum having the appropriate isospin and strangeness quantum numbers. However,  $\Sigma^*$  and  $\Xi^*$  correlation functions may have lower lying octet spin-1/2 components allowed by flavor-symmetry breaking,  $m_u = m_d \neq m_s$ . Therefore it is desirable to use the spin-3/2 projection operator [21]

$$P_{\mu\nu}^{3/2}(p) = g_{\mu\nu} - \frac{1}{3}\gamma_\mu\gamma_\nu - \frac{1}{3p^2}(\gamma \cdot p \gamma_\mu p_\nu + p_\mu \gamma_\nu \gamma \cdot p). \quad (2.18)$$

However, our precision results for baryon two-point functions give no indication of a low-lying spin-1/2 component being excited by the spin-3/2 interpolating fields, and conclude such excitations are negligible.

#### D. Three-point functions and multipole form factors

Here we begin with a brief overview of the results of Ref. [22], where the multipole form factors are defined

in terms of the covariant vertex functions and in terms of the current matrix elements. The electromagnetic current matrix element for spin-3/2 particles may be written as

$$\langle p', s' | j^\mu(0) | p, s \rangle = \sqrt{\frac{M_B^2}{E_p E_{p'}}} \bar{u}_\alpha(p', s') \mathcal{O}^{\alpha\mu\beta} u_\beta(p, s). \quad (2.19)$$

Here  $p$  and  $p'$  ( $s$  and  $s'$ ) denote the momentum (spin) of the initial and final states, respectively, and  $u_\alpha(p, s)$  is a Rarita-Schwinger spin-vector. The following Lorentz covariant form for the tensor

$$\mathcal{O}^{\alpha\mu\beta} = -g^{\alpha\beta} \left\{ a_1 \gamma^\mu + \frac{a_2}{2M_B} P^\mu \right\} - \frac{q^\alpha q^\beta}{(2M_B)^2} \left\{ c_1 \gamma^\mu + \frac{c_2}{2M_B} P^\mu \right\}, \quad (2.20)$$

where  $P = p' + p$ ,  $q = p' - p$  and  $M_B$  is the mass of the baryon, satisfies the standard requirements of invariance under time reversal, parity, G-parity and gauge transformations. The parameters  $a_1$ ,  $a_2$ ,  $c_1$  and  $c_2$  are independent covariant vertex functions.

---

The multipole form factors are defined in terms of the covariant vertex functions through the following Lorentz invariant expressions [22],

$$\mathcal{G}_{E0}(q^2) = (1 + \frac{2}{3}\tau) \{a_1 + (1 + \tau)a_2\} - \frac{1}{3}\tau(1 + \tau) \{c_1 + (1 + \tau)c_2\}, \quad (2.21)$$

$$\mathcal{G}_{E2}(q^2) = \{a_1 + (1 + \tau)a_2\} - \frac{1}{2}(1 + \tau) \{c_1 + (1 + \tau)c_2\}, \quad (2.22)$$

$$\mathcal{G}_{M1}(q^2) = (1 + \frac{4}{5}\tau)a_1 - \frac{2}{5}\tau(1 + \tau)c_1, \quad (2.23)$$

$$\mathcal{G}_{M3}(q^2) = a_1 - \frac{1}{2}(1 + \tau)c_1, \quad (2.24)$$

with  $\tau = -q^2/(2M_B)^2$  ( $\geq 0$ ). The multipole form factors  $\mathcal{G}_{E0}$ ,  $\mathcal{G}_{E2}$ ,  $\mathcal{G}_{M1}$  and  $\mathcal{G}_{M3}$  are referred to as charge ( $E0$ ), electric-quadrupole ( $E2$ ), magnetic-dipole ( $M1$ ) and magnetic-octupole ( $M3$ ) multipole form factors, respectively.

In a manner similar to that for the two-point function, the three-point Green function for the electromagnetic current is defined as

$$\langle G_{\sigma\tau}^{Bj^\mu B}(t_2, t_1; \vec{p}', \vec{p}; \Gamma) \rangle = \sum_{x_2, x_1} e^{-i\vec{p}' \cdot x_2} e^{+i(\vec{p}' - \vec{p}) \cdot x_1} \Gamma^{\beta\alpha} \langle \Omega | T(\chi_\sigma^\alpha(x_2) j^\mu(x_1) \bar{\chi}_\tau^\beta(0)) | \Omega \rangle. \quad (2.25)$$

Once again, the subscripts  $\sigma$ ,  $\tau$  are the Lorentz indices of the spin-3/2 interpolating fields. For large Euclidean time separations  $t_2 - t_1 \gg 1$  and  $t_1 \gg 1$  the three-point function at the hadronic level takes the limit

$$\langle G_{\sigma\tau}^{Bj^\mu B}(t_2, t_1; \vec{p}', \vec{p}; \Gamma) \rangle = \sum_{s, s'} e^{-E_{p'}(t_2 - t_1)} e^{-E_p t_1} \Gamma^{\beta\alpha} \langle \Omega | \chi_\sigma^\alpha | p', s' \rangle \langle p', s' | j^\mu | p, s \rangle \langle p, s | \bar{\chi}_\tau^\beta | \Omega \rangle, \quad (2.26)$$

where the matrix element of the electromagnetic current is defined in (2.19), and the matrix elements of the interpolating fields are defined by Eq. (2.10).

The time dependence of the three-point function may be eliminated through the use of the two-point functions. Maintaining the lattice Ward identity, which guarantees the lattice electric form factor reproduces the total charge of

the baryon at  $q^2 = 0$ , provides an indispensable guide to the optimum ratio of Green functions. The preferred ratio of two- and three-point Green functions is [7]

$$R_{\sigma}^{\mu}{}_{\tau}(t_2, t_1; \vec{p}', \vec{p}; \Gamma) = \left( \frac{\langle G_{\sigma\tau}^{Bj^{\mu}B}(t_2, t_1; \vec{p}', \vec{p}; \Gamma) \rangle \langle G_{\sigma\tau}^{Bj^{\mu}B}(t_2, t_1; -\vec{p}, -\vec{p}'; \Gamma) \rangle}{\langle G_{\sigma\tau}^{BB}(t_2; \vec{p}'; \Gamma_4) \rangle \langle G_{\sigma\tau}^{BB}(t_2; -\vec{p}; \Gamma_4) \rangle} \right)^{1/2}, \quad (2.27)$$

$$\simeq \left( \frac{E_p + M}{2E_p} \right)^{1/2} \left( \frac{E_{p'} + M}{2E_{p'}} \right)^{1/2} \bar{R}_{\sigma}^{\mu}{}_{\tau}(\vec{p}', \vec{p}; \Gamma), \quad (2.28)$$

where we have defined the reduced ratio  $\bar{R}_{\sigma}^{\mu}{}_{\tau}(\vec{p}', \vec{p}; \Gamma)$ . Note that there is no implied sum over  $\sigma$  and  $\tau$  in Eq. (2.27). Also, the square root in Eq. (2.27) spoils the covariant/contravariant nature of  $R_{\sigma}^{\mu}{}_{\tau}$  and no meaning should be attached to the location of the indices. We still prefer this notation due to the close connection with  $G_{\sigma\tau}^{Bj^{\mu}B}$ .

Using our standard definitions for  $\Gamma$  given in Eq. (2.12) and the Rarita-Schwinger spin sum of Eq. (2.11), the multipole form factors may be isolated and extracted from the following combinations of  $\bar{R}_{\sigma}^{\mu}{}_{\tau}(\vec{p}', \vec{p}; \Gamma)$

$$\mathcal{G}_{E0}(q^2) = \frac{1}{3} (\bar{R}_1^4{}_{11}(\vec{q}_1, 0; \Gamma_4) + \bar{R}_2^4{}_{22}(\vec{q}_1, 0; \Gamma_4) + \bar{R}_3^4{}_{33}(\vec{q}_1, 0; \Gamma_4)), \quad (2.29)$$

$$\mathcal{G}_{E2}(q^2) = 2 \frac{M(E+M)}{|\vec{q}_1|^2} (\bar{R}_1^4{}_{11}(\vec{q}_1, 0; \Gamma_4) + \bar{R}_2^4{}_{22}(\vec{q}_1, 0; \Gamma_4) - 2\bar{R}_3^4{}_{33}(\vec{q}_1, 0; \Gamma_4)), \quad (2.30)$$

$$\mathcal{G}_{M1}(q^2) = -\frac{3}{5} \frac{E+M}{|\vec{q}_1|} (\bar{R}_1^3{}_{11}(\vec{q}_1, 0; \Gamma_2) + \bar{R}_2^3{}_{22}(\vec{q}_1, 0; \Gamma_2) + \bar{R}_3^3{}_{33}(\vec{q}_1, 0; \Gamma_2)), \quad (2.31)$$

$$\mathcal{G}_{M3}(q^2) = -4 \frac{M(E+M)^2}{|\vec{q}_1|^3} \left( \bar{R}_1^3{}_{11}(\vec{q}_1, 0; \Gamma_2) + \bar{R}_2^3{}_{22}(\vec{q}_1, 0; \Gamma_2) - \frac{3}{2} \bar{R}_3^3{}_{33}(\vec{q}_1, 0; \Gamma_2) \right), \quad (2.32)$$

where  $\vec{q}_1 = (q, 0, 0)$ . We note that smaller statistical uncertainties may be obtained for  $\mathcal{G}_{E2}$  by using the symmetry

$$\bar{R}_2^4{}_{22}(\vec{q}_1, 0; \Gamma_4) = \bar{R}_3^4{}_{33}(\vec{q}_1, 0; \Gamma_4), \quad (2.33)$$

in Eq. (2.30). Hence, we define an average  $\bar{R}_{\text{avg}}^4$  as

$$\bar{R}_{\text{avg}}^4(\vec{q}_1, 0; \Gamma_4) = \frac{1}{2} [\bar{R}_2^4{}_{22}(\vec{q}_1, 0; \Gamma_4) + \bar{R}_3^4{}_{33}(\vec{q}_1, 0; \Gamma_4)]. \quad (2.34)$$

With this definition the expression for  $\mathcal{G}_{E2}(q^2)$  used in our simulations is

$$\mathcal{G}_{E2}(q^2) = 2 \frac{M(E+M)}{|\vec{q}_1|^2} \left( \bar{R}_1^4{}_{11}(\vec{q}_1, 0; \Gamma_4) - \bar{R}_{\text{avg}}^4(\vec{q}_1, 0; \Gamma_4) \right). \quad (2.35)$$

### III. LATTICE TECHNIQUES

The three-point functions discussed in section II are constructed using the sequential source technique outlined in Refs. [7, 23, 24]. Our quenched gauge fields are generated with the  $\mathcal{O}(a^2)$  mean-field improved Lüscher-Weisz plaquette plus rectangle gauge action [25] using the plaquette measure for the mean link. The simulations are performed on a  $20^3 \times 40$  lattice with a lattice spacing of 0.128 fm as determined by the Sommer scale [26]  $r_0 = 0.50$  fm. This large volume lattice ensures a good density of low-lying momenta which are key to giving rise to chiral non-analytic behavior in the observables simulated on the lattice [10, 11].

We perform a high-statistics analysis using a large sample of 400 configurations for our lightest eight quark masses. We also consider a subset of 200 configurations

---

for our three heaviest quark masses to explore the approach to the heavy-quark regime. A small sub-ensemble bias correction is applied multiplicatively to the heavy quark results, by matching the central values of the 200 configuration sub-ensemble and 400 configuration ensemble averages at  $\kappa = 0.12780$ . All tables display the raw, unbiased data for the first four kappa values. The first row of the  $\kappa = 0.12780$  results gives the results from the 200 configuration sub-ensembles, the second gives the 400 configuration ensemble results. The scaled results from the 200 configuration sub-ensembles are shown in the figures.

We use the fat-link irrelevant clover (FLIC) Dirac operator [27] which provides  $\mathcal{O}(a)$  improvement [28]. The improved chiral properties of FLIC fermions allow efficient access to the light quark-mass regime [29], making them ideal for dynamical fermion simulations now under-

way [30]. For the vector current, we use an  $\mathcal{O}(a)$ -improved FLIC conserved vector current [14]. We use a smeared source at  $t_0 = 8$ , and a current insertion centered at  $t_1 = 14$ . Complete details are described in Ref. [14].

Table I provides the kappa values used in our simulations, together with the calculated  $\pi$  and decuplet baryon masses. While we refer to  $m_\pi^2$  to infer the quark masses, we note that the critical value where the pion mass vanishes is  $\kappa_{\text{cr}} = 0.13135$ .

We select  $\kappa = 0.12885$  to represent the strange quark in this simulation. At this  $\kappa$  the  $s\bar{s}$  pseudo scalar mass is 0.697 GeV, which compares well with the experimental value of  $2m_K^2 - m_\pi^2 = (0.693 \text{ GeV})^2$ , motivated by leading order chiral perturbation theory.

The error analysis of the correlation function ratios is performed via a third-order, single-elimination jackknife, with the  $\chi^2$  per degree of freedom ( $\chi_{\text{dof}}^2$ ) obtained via covariance matrix fits. We perform a series of fits through the ratios after the current insertion at  $t_1 = 14$ . By examining the  $\chi_{\text{dof}}^2$  we are able to establish a valid window through which we may fit in order to extract our observables. In all cases, we required a value of  $\chi_{\text{dof}}^2$  no larger than 1.5. The values of the static quantities quoted in this paper on a per quark-sector basis correspond to values for single quarks of unit charge.

When extracting form factors from the lattice correlation functions via the ratios defined in Eqs. (2.29) to (2.32) in Sec. II D, we employ the advanced analysis techniques outlined in detail in Ref. [14].

The following calculations are performed in the lab frame  $\vec{p} = 0$ ,  $\vec{p}' = \vec{q} = |\vec{q}|\hat{x}$  at  $|\vec{q}|a = 2\pi/L_x$  with  $L_x = 20$ , the minimum nonzero momentum available on our lattice. While  $q^2$  is dependent on the mass of the baryon, we find this mass dependence to be small. Indeed all form factors may be regarded as being calculated at  $Q^2 = -q^2 = 0.230 \pm 0.001 \text{ GeV}^2$  where the error is dominated by the mass dependence of the target baryon. Where a spatial direction of the electromagnetic current is required, it is chosen to be the  $z$ -direction.

## IV. CORRELATION FUNCTION ANALYSIS

### A. Baryon Masses

Figure 2 is a plot of the decuplet baryon masses along with the masses of the octet baryon from our previous calculation [14]. We observe the  $SU(3)_{\text{flavor}}$  limit at our sixth quark mass when  $m_\pi^2 = 0.485(3) \text{ GeV}^2$ . The mass of the  $\Omega^-$  is the mass of the  $\Delta$  at the  $SU(3)_{\text{flavor}}$  limit, i.e.,  $1.732 \pm 0.012 \text{ GeV}$  which differs from the experimentally measured value of 1.67 GeV by only about 3.6%. The higher value from the quenched simulation is in accord with the expectations of quenched  $\chi\text{EFT}$  [31, 32]. The mass of the  $\Delta$  baryon shows an upward chiral curvature as the  $m_\pi^2$  becomes smaller. This behavior has already been discussed in Refs. [29, 31, 33].

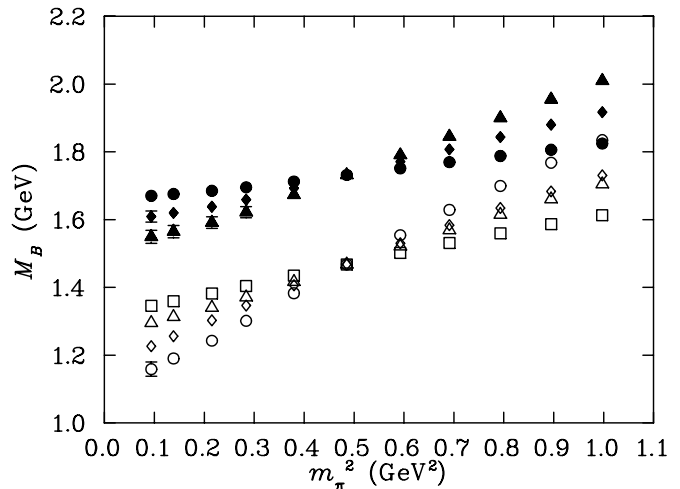


FIG. 2: Masses of the decuplet and the octet baryons [14] at different quark masses. The octet baryon masses are the open symbols while the symbols of the decuplet baryons are filled. At the lowest quark mass the lowest point is the Nucleon, followed by  $\Lambda$ ,  $\Sigma$  and the  $\Xi$ . The decuplet baryon with lowest mass is the  $\Delta$  followed by  $\Sigma^*$  and  $\Xi^*$ .

### B. Form Factor Correlators

The baryon form factors are calculated on a quark-sector by quark-sector basis with each sector normalized to the contribution of a single quark with unit charge. Hence to calculate the corresponding baryon property, each quark sector contribution should be multiplied by the appropriate charge and quark number. Under such a scheme for a generic form factor  $f$ , the  $\Delta^+$  form factor,  $f_{\Delta^+}$ , is obtained from the  $u$ - and  $d$ -quark sectors normalized for a single quark of unit charge via

$$f_{\Delta^+} = 2 \times \frac{2}{3} \times f_u + 1 \times \left(-\frac{1}{3}\right) \times f_d. \quad (4.1)$$

Figure 3 depicts the electric form factor  $E0$  of the  $u$  quark in the  $\Delta$  as a function of time at the  $SU(3)_{\text{flavor}}$  limit. The  $u$  and  $d$  quarks in the  $\Delta$  states are identical as discussed in regard to Eq. (2.7). The straight lines indicate the fits which were selected using the  $\chi_{\text{dof}}^2$  considerations outlined in Ref. [14]. For light quark masses smaller than the strange quark mass, we fit the change in the form factor correlation functions from one quark mass to the next and add this to the previous result at the heavier quark mass. This provides significant cancellation of correlated systematic errors and makes the selection of the fit regime transparent.

Figure 4 shows the fitting of the electric form factor splitting for the  $\Delta^+$  between the eighth and ninth quark masses, the latter having  $m_\pi^2 = 0.215(4) \text{ GeV}^2$ . The improvement of the plateau is apparent in Fig. 4. Still substantial Euclidean time evolution is required to obtain an acceptable  $\chi_{\text{dof}}^2$ .

TABLE I: Hadron masses in units of GeV for various values of the hopping parameter,  $\kappa$ . Pion masses are in  $\text{GeV}^2$  while the baryon masses are in GeV.

$\kappa$	$m_\pi^2$	$\Delta$	$\Sigma^*$	$\Xi^*$
0.12630	0.9960(56)	1.999(9)	1.908(10)	1.815(11)
0.12680	0.8936(56)	1.945(10)	1.871(11)	1.797(12)
0.12730	0.7920(55)	1.890(10)	1.834(11)	1.779(13)
0.12780	0.6920(54)	1.836(11)	1.798(12)	1.761(13)
0.12780	0.6910(35)	1.845(10)	1.807(11)	1.770(11)
0.12830	0.5925(33)	1.791(11)	1.771(11)	1.752(12)
0.12885	0.4854(31)	1.732(12)	1.732(12)	1.732(12)
0.12940	0.3795(31)	1.673(14)	1.693(13)	1.712(13)
0.12990	0.2839(33)	1.622(16)	1.659(15)	1.695(13)
0.13205	0.2153(35)	1.592(17)	1.638(15)	1.685(13)
0.13060	0.1384(43)	1.565(18)	1.620(16)	1.676(14)
0.13080	0.0939(44)	1.549(19)	1.609(16)	1.670(14)
experiment	0.0196	1.232	1.382	1.531

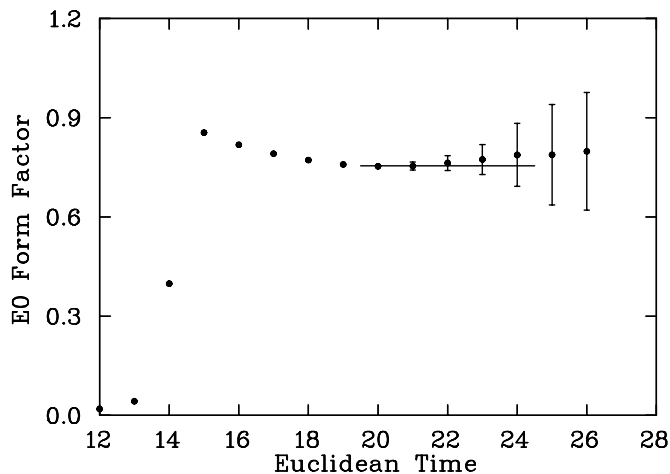


FIG. 3:  $E0$  electric form factor of the  $u$  quark in the  $\Delta$  at  $Q^2 = 0.230(1) \text{ GeV}^2$  as a function of Euclidean time ( $t_2$ ) for  $m_\pi^2 = 0.4854 \text{ GeV}^2$ , the  $SU(3)_{\text{flavor}}$  limit. The line indicates the fitting window and the best fit value.

Tables II to IV list the electric form factors for all the decuplet baryons at the quark level for the eleven quark masses considered. In the tables, the selected time frame, the fit value and the associated  $\chi_{\text{dof}}^2$  are indicated. Table V provides collected results for the various decuplet baryons.

The magnetic form factor  $M1$  for the  $u$  quark sector in the  $\Delta$  at the  $SU(3)$  limit is plotted in Fig. 5 as a function of Euclidean time. Here the conversion from the natural magneton,  $e/(2m_B)$ , where the mass of the baryon under investigation appears, to the nuclear magneton,  $e/(2m_N)$ , where the physical nucleon mass appears, has been done by multiplying the lattice form factor results by the ratio  $m_N/m_B$ . In this way the form factors are

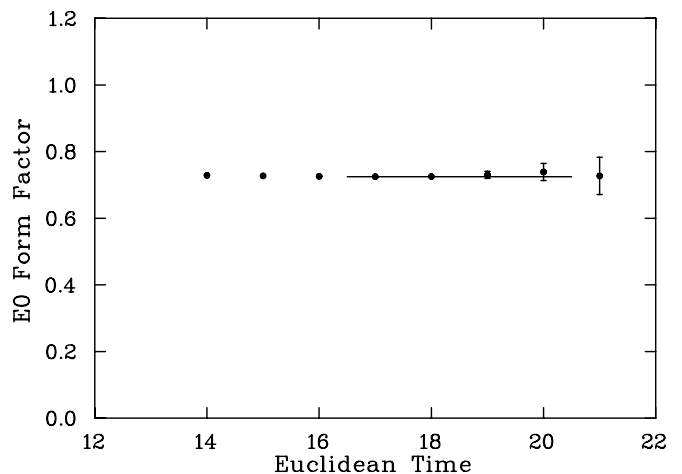


FIG. 4:  $E0$  electric form factor of the  $u$  quark in the  $\Delta$  at  $Q^2 = 0.230(1) \text{ GeV}^2$  as a function of Euclidean time ( $t_2$ ) at the ninth quark mass where  $m_\pi^2 = 0.215(4) \text{ GeV}^2$ . The correlator is obtained from the splitting between the ninth and eighth quark mass results. The line indicates the fitting window and the best fit value.

presented in terms of a constant unit; *i.e.* the nuclear magneton.

In Fig. 6 we present the Euclidean time dependence of the the  $M1$  magnetic form factors of  $\Delta$  calculated at the ninth quark mass where  $m_\pi^2 = 0.215(4) \text{ GeV}^2$  using the splittings analysis. The onset of noise at this lighter quark mass is particularly apparent at time slice 20.

Results for the quark-sector contributions to the  $M1$  magnetic form factors of decuplet baryons are summarized in Tables VI to VIII. While some of the  $\chi_{\text{dof}}^2$  are some what large we note that neighboring regimes with acceptable  $\chi_{\text{dof}}^2$  have a variation in the central value that



TABLE II: Quark sector contributions to the electric form factor  $E0$  of the  $\Delta$  at  $Q^2 = 0.230(1)$  GeV<sup>2</sup>. Sector contributions are for a single quark of unit charge. The fit windows are selected using the criteria outlined in Ref. [14]. The quark contribution at the SU(3) limit when  $m_\pi^2 = 0.485(3)$  GeV<sup>2</sup> provides the  $s$  quark contribution in  $\Omega^-$ .

$m_\pi^2$ (GeV <sup>2</sup> )	fit value	$u_\Delta$ fit window	$\chi_{\text{dof}}^2$	fit value	$d_\Delta$ fit window	$\chi_{\text{dof}}^2$
0.9960(56)	0.800(5)	20 – 24	1.47	0.800(5)	20 – 24	1.47
0.8936(56)	0.794(6)	20 – 24	0.95	0.794(6)	20 – 24	0.95
0.7920(55)	0.788(7)	20 – 24	0.79	0.788(7)	20 – 24	0.79
0.6920(54)	0.783(8)	20 – 24	0.59	0.783(8)	20 – 24	0.59
0.6910(35)	0.773(6)	20 – 24	1.46	0.773(6)	20 – 24	1.46
0.5925(33)	0.764(7)	20 – 24	1.07	0.764(7)	20 – 24	1.07
0.4854(31)	0.755(10)	20 – 24	0.53	0.755(10)	20 – 24	0.53
0.3795(31)	0.744(11)	17 – 20	0.73	0.744(11)	17 – 20	0.73
0.2839(33)	0.733(13)	17 – 20	0.79	0.733(13)	17 – 20	0.79
0.2153(35)	0.725(16)	17 – 19	0.46	0.725(16)	17 – 19	0.46
0.1384(43)	0.717(22)	17 – 19	0.23	0.717(22)	17 – 19	0.23
0.0939(44)	0.693(33)	17 – 19	0.34	0.693(33)	17 – 19	0.34

TABLE III: Quark sector contributions to the electric form factor  $E0$  of  $\Sigma^*$  at  $Q^2 = 0.230(1)$  GeV<sup>2</sup>. Sector contributions are for a single quark having unit charge. The fit windows are selected using the criteria outlined in Ref. [14].

$m_\pi^2$ (GeV <sup>2</sup> )	fit value	$u_{\Sigma^*}$ or $d_{\Sigma^*}$ fit window	$\chi_{\text{dof}}^2$	fit value	$s_{\Sigma^*}$ fit window	$\chi_{\text{dof}}^2$
0.9960(56)	0.804(6)	20 – 24	0.85	0.759(9)	20 – 24	0.54
0.8936(56)	0.798(7)	20 – 24	0.65	0.761(9)	20 – 24	0.50
0.7920(55)	0.792(8)	20 – 24	0.63	0.763(10)	20 – 24	0.49
0.6920(54)	0.786(9)	20 – 24	0.56	0.766(10)	20 – 24	0.48
0.6910(35)	0.774(6)	20 – 24	1.15	0.752(8)	20 – 24	0.97
0.5925(33)	0.764(8)	20 – 24	0.91	0.753(8)	20 – 24	0.79
0.4854(31)	0.755(10)	20 – 24	0.53	0.755(10)	20 – 24	0.53
0.3795(31)	0.744(11)	17 – 20	0.89	0.754(10)	17 – 20	0.22
0.2839(33)	0.733(12)	17 – 20	0.81	0.754(11)	17 – 20	0.37
0.2153(35)	0.727(14)	17 – 19	0.15	0.753(11)	17 – 19	0.21
0.1384(43)	0.719(18)	17 – 19	0.07	0.753(12)	17 – 19	0.05
0.0939(44)	0.710(23)	17 – 19	0.22	0.746(14)	17 – 19	0.63

is small with respect to the statistical uncertainty. Results for the various decuplet baryons are given in Table IX.

## V. DISCUSSION OF RESULTS

### A. Charge radii

It is well known that the experimental electric (and magnetic) form factor of the proton is described well by a dipole ansatz at small  $Q^2$

$$\mathcal{G}_E(Q^2) = \frac{\mathcal{G}_E(0)}{(1 + Q^2/m^2)^2}; \quad Q^2 \geq 0. \quad (5.1)$$

This behavior has also been observed in recent lattice calculations [34]. Using this observation, together with the standard small  $Q^2$  expansion of the Fourier transform of a spherical charge distribution

$$\langle r_E^2 \rangle = -6 \frac{d}{dQ^2} \mathcal{G}_E(Q^2) \Big|_{Q^2=0}, \quad (5.2)$$

we arrive at an expression which allows us to calculate the electric charge radius of a baryon using our two available values of the Sachs electric form factor ( $\mathcal{G}_E(Q_{\text{min}}^2)$ ,  $\mathcal{G}_E(0)$ ), namely

$$\frac{\langle r_E^2 \rangle}{\mathcal{G}_E(0)} = \frac{12}{Q^2} \left( \sqrt{\frac{\mathcal{G}_E(0)}{\mathcal{G}_E(Q^2)}} - 1 \right). \quad (5.3)$$

TABLE IV: Quark sector contributions to the electric form factor  $E0$  of  $\Xi^*$  at  $Q^2 = 0.230(1)$  GeV<sup>2</sup>. Sector contributions are for a single quark having unit charge. The fit windows are selected using the criteria outlined in Ref. [14].

$m_\pi^2$ (GeV <sup>2</sup> )	fit value	$s_{\Xi^*}$ fit window	$\chi_{\text{dof}}^2$	fit value	$u_{\Xi^*}$ fit window	$\chi_{\text{dof}}^2$
0.9960(56)	0.765(10)	20 – 24	0.47	0.809(8)	20 – 24	0.66
0.8936(56)	0.766(11)	20 – 24	0.47	0.802(8)	20 – 24	0.58
0.7920(55)	0.767(11)	20 – 24	0.49	0.795(9)	20 – 24	0.61
0.6920(54)	0.769(12)	20 – 24	0.50	0.788(10)	20 – 24	0.58
0.6910(35)	0.753(9)	20 – 24	0.73	0.775(7)	20 – 24	0.89
0.5925(33)	0.754(9)	20 – 24	0.66	0.765(8)	20 – 24	0.75
0.4854(31)	0.755(10)	20 – 24	0.53	0.755(10)	20 – 24	0.53
0.3795(31)	0.754(10)	17 – 20	0.19	0.744(10)	17 – 20	1.19
0.2839(33)	0.754(10)	17 – 20	0.22	0.734(11)	17 – 20	0.77
0.2153(35)	0.754(10)	17 – 19	0.03	0.727(13)	17 – 19	0.09
0.1384(43)	0.755(11)	17 – 19	0.11	0.720(14)	17 – 19	0.10
0.0939(44)	0.754(11)	17 – 19	0.66	0.714(17)	17 – 19	0.19

TABLE V:  $E0$  form factor of the charged decuplet baryons for different  $m_\pi^2$  values. The  $E0$  form factor of the  $\Delta^-$  at the  $SU(3)_{\text{flavor}}$  limit ( $m_\pi^2 = 0.485(3)$  GeV<sup>2</sup>) provides the  $E0$  form factor of  $\Omega^-$ .

$m_\pi^2$ (GeV <sup>2</sup> )	$\Delta^{++}$	$\Delta^+$	$\Delta^-$	$\Sigma^{*+}$	$\Sigma^{*-}$	$\Xi^{*-}$
0.9972(55)	1.601(10)	0.803(5)	-0.803(5)	0.819(6)	-0.789(7)	-0.780(9)
0.8936(56)	1.589(11)	0.794(6)	-0.794(6)	0.810(6)	-0.786(7)	-0.778(10)
0.7920(55)	1.577(13)	0.788(7)	-0.788(7)	0.801(7)	-0.782(8)	-0.777(10)
0.6920(54)	1.566(16)	0.783(8)	-0.783(8)	0.792(8)	-0.779(9)	-0.775(11)
0.6910(35)	1.545(11)	0.773(6)	-0.773(6)	0.781(6)	-0.766(7)	-0.760(8)
0.5925(33)	1.527(14)	0.764(7)	-0.764(7)	0.768(7)	-0.761(8)	-0.757(9)
0.4854(31)	1.509(19)	0.755(10)	-0.755(10)	0.755(10)	-0.755(10)	-0.755(10)
0.3795(31)	1.487(22)	0.744(11)	-0.744(11)	0.740(11)	-0.747(10)	-0.751(10)
0.2839(33)	1.465(26)	0.733(13)	-0.733(13)	0.726(13)	-0.741(12)	-0.747(11)
0.2153(35)	1.451(31)	0.725(16)	-0.725(16)	0.718(15)	-0.736(13)	-0.745(11)
0.1384(43)	1.433(44)	0.717(22)	-0.717(22)	0.708(20)	-0.730(15)	-0.743(12)
0.0939(44)	1.386(65)	0.693(33)	-0.693(33)	0.698(27)	-0.722(19)	-0.741(13)

However to calculate the charge radii of the neutral baryons, the above equation cannot be used, due to the fact that in those cases  $\mathcal{G}_E = 0$ . For the neutral baryons it becomes a simple matter to construct the charge radii by first calculating the charge radii for each quark sector. These quark sectors are then combined using the appropriate charge and quark number factors as described in Sec. IV B to obtain the total baryon charge radii. Indeed, all baryon charge radii including the charged states are calculated in this manner.

Tables X to XII provide the electric charge radii of the decuplet baryons and the quark sector contributions. Figures 7 and 8 depict plots of the quark contributions to the decuplet charge radii. At the  $SU(3)$  limit (sixth quark mass) the quark contributions are identical in all cases as expected.

In Figs. 9 and 10 we compare the charge radii of the

quark sectors in the decuplet baryons to those in the octet baryons at the ninth quark mass. From the figures it is evident that the contribution of the quarks is very much baryon dependent in the octet case, while for the decuplet baryons there is much less environmental sensitivity to the individual quark contributions. More specifically, in the case of the  $u$  quark in the octet baryons, the charge radius decreases with the inclusion of the  $s$  quark, while such an influence of the  $s$  quark on  $u$  quark charge radius is absent in the decuplet behavior. Furthermore, we note that the charge radius of the  $u$  quark distribution in the decuplet baryons is *smaller* than that in the octet baryons.

From Fig. 9 it is evident that the charge radius of the  $u$  quark in the proton ( $u_p$ ) is larger than that of the  $u$  quark in the  $\Delta^+$  ( $u_{\Delta^+}$ ). In order to investigate this difference more accurately, we compute the ratios of charge distri-

TABLE VI: Quark sector contributions to the magnetic form factor  $M1$  of  $\Delta$  at  $Q^2 = 0.230(1)$  GeV<sup>2</sup>. Sector contributions are for a single quark having unit charge. The fit windows are selected using the criteria outlined in Ref. [14]. The quark contribution at the  $SU(3)_{\text{flavor}}$  limit when  $m_\pi^2 = 0.4854(31)$  GeV<sup>2</sup> provides the  $s$  quark contribution in  $\Omega^-$ .

$m_\pi^2$ (GeV <sup>2</sup> )	$u_\Delta$ ( $\mu_N$ )			$d_\Delta$ ( $\mu_N$ )		
	fit value	fit window	$\chi_{\text{dof}}^2$	fit value	fit window	$\chi_{\text{dof}}^2$
0.9960(56)	1.173(25)	19 – 24	1.45	1.173(25)	19 – 24	1.45
0.8936(56)	1.201(29)	19 – 24	1.14	1.201(29)	19 – 24	1.14
0.7920(55)	1.230(33)	19 – 24	0.95	1.230(33)	19 – 24	0.95
0.6920(54)	1.256(40)	19 – 24	0.75	1.256(40)	19 – 24	0.75
0.6910(35)	1.248(32)	19 – 24	1.25	1.248(32)	19 – 24	1.25
0.5925(33)	1.269(41)	19 – 24	0.79	1.269(41)	19 – 24	0.79
0.4854(31)	1.280(56)	19 – 24	0.31	1.280(56)	19 – 24	0.31
0.3795(31)	1.301(64)	17 – 21	1.37	1.301(64)	17 – 21	1.37
0.2839(33)	1.312(75)	17 – 19	1.14	1.312(75)	17 – 19	1.14
0.2153(35)	1.309(89)	17 – 19	0.91	1.309(89)	17 – 19	0.91
0.1384(43)	1.28(12)	17 – 18	1.26	1.28(12)	17 – 18	1.26
0.0939(44)	1.11(21)	17 – 18	1.79	1.11(21)	17 – 18	1.79

TABLE VII: Quark sector contributions to the magnetic form factor  $M1$  of  $\Sigma^*$  at  $Q^2 = 0.230(1)$  GeV<sup>2</sup>. Sector contributions are for a single quark having unit charge. The fit windows are selected using the criteria outlined in Ref. [14].

$m_\pi^2$ (GeV <sup>2</sup> )	$u_{\Sigma^*}$ or $d_{\Sigma^*}$ ( $\mu_N$ )			$s_{\Sigma^*}$ ( $\mu_N$ )		
	fit value	fit window	$\chi_{\text{dof}}^2$	fit value	fit window	$\chi_{\text{dof}}^2$
0.9960(56)	1.191(31)	19 – 24	1.07	1.268(40)	19 – 24	0.51
0.8936(56)	1.216(35)	19 – 24	0.90	1.275(42)	19 – 24	0.49
0.7920(55)	1.242(39)	19 – 24	0.82	1.282(45)	19 – 24	0.47
0.6920(54)	1.264(45)	19 – 24	0.69	1.289(50)	19 – 24	0.47
0.6910(35)	1.254(37)	19 – 24	0.94	1.275(41)	19 – 24	0.69
0.5925(33)	1.272(45)	19 – 24	0.64	1.278(47)	19 – 24	0.51
0.4854(31)	1.280(56)	19 – 24	0.31	1.280(56)	19 – 24	0.31
0.3795(31)	1.297(62)	17 – 21	1.72	1.289(60)	17 – 21	0.70
0.2839(33)	1.306(68)	17 – 19	1.88	1.299(65)	17 – 19	0.04
0.2153(35)	1.305(76)	17 – 19	1.84	1.309(69)	17 – 19	0.08
0.1384(43)	1.299(89)	17 – 19	3.44	1.330(74)	17 – 19	0.44
0.0939(44)	1.25(12)	17 – 18	2.55	1.303(88)	17 – 18	0.16

butions of similar quarks in the octet to that in the decuplet. The uncertainty in the ratio  $\langle r^2 \rangle(u_p) / \langle r^2 \rangle(u_{\Delta^+})$  is calculated using the jack-knife method. Figures 11 and 12 depict the ratio of the quark contributions in the octet baryons to those in the decuplet baryons at the  $SU(3)_{\text{flavor}}$  limit and the ninth quark mass, respectively. In both cases, the doubly represented  $u$  quark contribution to the charge radius of octet baryons is larger than that in case of the singly represented octet quarks and decuplet quarks. At the  $SU(3)$  limit, all quarks take the strange quark mass, and hence one would expect the quark model picture to dominate. This suggests that the  $u_\Delta$  should have a broader distribution than the distribution than that of  $u_p$  due to hyperfine interactions.

Our results contrast this prediction. The smaller charge radius of  $u_\Delta$  compared to that of  $u_p$  also rules out any suggestion of a hyperfine attraction leading to  $ud$  diquark clustering in the nucleon or hyperon states [35].

The charge radii of the various decuplet baryon states are shown in Figs. 13, 14 and 15 as a function of  $m_\pi^2$ . The charge radius of  $\Delta^-$  is numerically equal to that of the  $\Delta^+$  with a negative sign. The charge radius of  $\Omega^-$  is taken as that of the  $\Delta^-$  in the  $SU(3)_{\text{flavor}}$  limit, and is numerically equal to  $-0.307 \pm 0.015$  fm<sup>2</sup>. As our calculations neglect the  $\Omega^- \rightarrow \Xi^0 \pi^-$  dressing, we anticipate our result to underestimate the magnitude.

The decuplet baryon form factors are dominated by the net charge of the light quarks. For the  $\Delta^0$  the symmetry

TABLE VIII: Quark sector contributions to the magnetic form factor  $M1$  of  $\Xi^*$  at  $Q^2 = 0.230(1)$  GeV<sup>2</sup>. Sector contributions are for a single quark having unit charge. The fit windows are selected using the criteria outlined in Ref. [14].

$m_\pi^2$ (GeV <sup>2</sup> )	$s_{\Xi^*}$ ( $\mu_N$ )			$u_{\Xi^*}$ or $d_{\Xi^*}$ ( $\mu_N$ )		
	fit value	fit window	$\chi_{\text{dof}}^2$	fit value	fit window	$\chi_{\text{dof}}^2$
0.9960(56)	1.286(50)	19 – 24	0.45	1.208(39)	19 – 24	0.84
0.8936(56)	1.289(52)	19 – 24	0.46	1.231(42)	19 – 24	0.79
0.7920(55)	1.293(54)	19 – 24	0.46	1.254(46)	19 – 24	0.76
0.6920(54)	1.297(56)	19 – 24	0.45	1.273(51)	19 – 24	0.63
0.6910(35)	1.278(48)	19 – 24	0.48	1.260(44)	19 – 24	0.68
0.5925(33)	1.280(51)	19 – 24	0.40	1.274(49)	19 – 24	0.52
0.4854(31)	1.280(56)	19 – 24	0.31	1.280(56)	19 – 24	0.31
0.3795(31)	1.285(58)	17 – 21	0.70	1.293(60)	17 – 21	2.56
0.2839(33)	1.289(60)	17 – 19	0.04	1.300(63)	17 – 19	2.66
0.2153(35)	1.293(62)	17 – 19	0.02	1.303(66)	17 – 19	1.44
0.1384(43)	1.302(64)	17 – 18	0.73	1.303(72)	17 – 18	2.36
0.0939(44)	1.301(67)	17 – 18	0.23	1.313(81)	17 – 18	0.56

TABLE IX:  $M1$  form factor of the charged decuplet baryons for different  $m_\pi^2$  values. The  $M1$  form factor of the  $\Delta^-$  at the  $SU(3)_{\text{flavor}}$  limit ( $m_\pi^2 = 0.485(3)$  GeV<sup>2</sup>) provides the  $M1$  form factor of  $\Omega^-$ .

$m_\pi^2$ (GeV <sup>2</sup> )	$\Delta^{++}$	$\Delta^+$	$\Delta^-$	$\Sigma^{*+}$	$\Sigma^{*-}$	$\Xi^{*-}$
0.9972(55)	2.35(5)	1.17(2)	-1.17(2)	1.16(3)	-1.22(3)	-1.26(5)
0.8936(56)	2.40(6)	1.20(3)	-1.20(3)	1.20(3)	-1.24(4)	-1.27(5)
0.7920(55)	2.46(7)	1.23(3)	-1.23(3)	1.23(4)	-1.26(4)	-1.28(5)
0.6920(54)	2.51(8)	1.26(4)	-1.26(4)	1.26(4)	-1.27(4)	-1.29(5)
0.6910(35)	2.50(6)	1.25(3)	-1.25(3)	1.25(4)	-1.26(4)	-1.27(5)
0.5925(33)	2.54(8)	1.27(4)	-1.27(4)	1.27(4)	-1.27(5)	-1.28(5)
0.4854(31)	2.56(11)	1.28(6)	-1.28(6)	1.28(6)	-1.28(6)	-1.28(6)
0.3795(31)	2.60(13)	1.30(6)	-1.30(6)	1.30(6)	-1.29(6)	-1.29(6)
0.2839(33)	2.62(15)	1.31(7)	-1.31(7)	1.31(7)	-1.30(7)	-1.29(6)
0.2153(35)	2.62(18)	1.31(9)	-1.31(9)	1.30(8)	-1.31(7)	-1.30(6)
0.1384(43)	2.56(24)	1.28(12)	-1.28(12)	1.29(10)	-1.31(8)	-1.30(6)
0.0939(44)	2.22(43)	1.11(22)	-1.11(22)	1.23(14)	-1.27(10)	-1.30(7)

of the  $u$  and  $d$  quarks makes the form factors vanish. This is in contrast to the neutron where the three quarks are in mixed-symmetric states, giving rise to a non-zero form factor and charge radius. Charge radii of the neutral  $\Sigma^*$  and  $\Xi^*$  are also close to zero and are dominated by the light quark sectors.

The presence of the  $s$  quark as one moves from  $\Delta$  to  $\Sigma^*$  and  $\Xi^*$  reduces the magnitude of the charge radius as indicated in Figs. 13, 14 and 15. By examining the ratio of the charge radii of the octet to decuplet baryons in Fig. 16, we observe that the octet baryons have a slightly larger charge radius than their decuplet counterparts.

## B. Magnetic moments

The magnetic moment is provided by the value of the magnetic form factor at zero momentum transfer,  $Q^2 = 0$ ,

$$\mu = \mathcal{G}_M(0) \frac{e}{2M_B}, \quad (5.4)$$

in units of the natural magneton, where  $M_B$  is the mass of the baryon. Since the magnetic form factors must be calculated at a finite value of momentum transfer,  $Q^2$ , the magnetic moment must be inferred from our results,  $\mathcal{G}_M(Q^2)$ , obtained at the minimum non-vanishing momentum transfer available on our periodic lattice. We choose to scale our results from  $\mathcal{G}_M(Q^2)$  to  $\mathcal{G}_M(0)$ . We do this by assuming that the  $Q^2$  dependence of the electric and magnetic form factors are similar at the quark

TABLE X: Charge radii of the  $\Delta$  baryons for different  $m_\pi^2$ . Quark sector contributions for a single quark of unit charge are included. The charge radii of the  $\Delta^{++}$  are twice that of the  $\Delta^+$  and the results for the  $\Delta^0$  are 0 in QCD. At the  $SU(3)_{\text{flavor}}$  limit we find the charge radius of the  $\Omega^-$  to be equal to  $-0.307(15) \text{ fm}^2$ .

$m_\pi^2(\text{GeV}^2)$	$u_\Delta(\text{fm}^2)$	$d_\Delta(\text{fm}^2)$	$\Delta^+(\text{fm}^2)$	$\Delta^-(\text{fm}^2)$
0.9960(56)	0.238(7)	0.238(7)	0.238(7)	-0.238(7)
0.8936(56)	0.247(8)	0.247(8)	0.247(8)	-0.247(8)
0.7920(55)	0.256(10)	0.256(10)	0.256(10)	-0.256(10)
0.6920(54)	0.264(12)	0.264(12)	0.264(12)	-0.264(12)
0.6910(35)	0.279(9)	0.279(9)	0.279(9)	-0.279(9)
0.5925(33)	0.293(11)	0.293(11)	0.293(11)	-0.293(11)
0.4854(31)	0.307(15)	0.307(15)	0.307(15)	-0.307(15)
0.3795(31)	0.324(17)	0.324(17)	0.324(17)	-0.324(17)
0.2839(33)	0.343(21)	0.343(21)	0.343(21)	-0.343(21)
0.2153(35)	0.355(26)	0.355(26)	0.355(26)	-0.355(26)
0.1384(43)	0.370(37)	0.370(37)	0.370(37)	-0.370(37)
0.0939(44)	0.410(57)	0.410(57)	0.410(57)	-0.410(57)

TABLE XI: Charge radii of the  $\Sigma^*$  baryons for different  $m_\pi^2$ . Quark sector contributions for a single quark of unit charge are included.

$m_\pi^2(\text{GeV}^2)$	$u_{\Sigma^*}(\text{fm}^2)$	$s_{\Sigma^*}(\text{fm}^2)$	$\Sigma^{*+}(\text{fm}^2)$	$\Sigma^{*0}(\text{fm}^2)$	$\Sigma^{*-}(\text{fm}^2)$
0.9960(56)	0.233(8)	0.299(13)	0.212(8)	-0.022(3)	-0.255(10)
0.8936(56)	0.242(10)	0.296(14)	0.224(9)	-0.018(2)	-0.260(11)
0.7920(55)	0.251(11)	0.293(15)	0.237(10)	-0.014(2)	-0.265(12)
0.6920(54)	0.260(13)	0.289(16)	0.250(12)	-0.010(2)	-0.270(14)
0.6910(35)	0.278(10)	0.311(12)	0.267(9)	-0.011(1)	-0.289(10)
0.5925(33)	0.292(12)	0.309(13)	0.286(11)	-0.006(1)	-0.298(12)
0.4854(31)	0.307(15)	0.307(15)	0.307(15)	0.000(1)	-0.307(15)
0.3795(31)	0.324(17)	0.308(16)	0.330(17)	0.006(1)	-0.319(16)
0.2839(33)	0.341(20)	0.309(17)	0.352(21)	0.011(1)	-0.330(19)
0.2153(35)	0.352(23)	0.309(17)	0.366(25)	0.014(2)	-0.338(21)
0.1384(43)	0.365(29)	0.311(18)	0.383(33)	0.018(5)	-0.347(25)
0.0939(44)	0.380(39)	0.321(22)	0.399(45)	0.020(7)	-0.360(32)

TABLE XII: Charge radii of the  $\Xi^*$  baryons for different  $m_\pi^2$  values. Quark sector contributions for a single quark of unit charge are included.

$m_\pi^2(\text{GeV}^2)$	$s_{\Xi^*}(\text{fm}^2)$	$u_{\Xi^*}(\text{fm}^2)$	$\Xi^{*0}(\text{fm}^2)$	$\Xi^{*-}(\text{fm}^2)$
0.9960(56)	0.291(16)	0.227(11)	-0.042(5)	-0.269(14)
0.8936(56)	0.289(16)	0.236(12)	-0.035(5)	-0.271(14)
0.7920(55)	0.287(17)	0.246(13)	-0.027(4)	-0.273(15)
0.6920(54)	0.285(17)	0.256(14)	-0.019(3)	-0.275(16)
0.6910(35)	0.309(13)	0.276(11)	-0.022(3)	-0.298(12)
0.5925(33)	0.308(14)	0.291(13)	-0.011(2)	-0.302(14)
0.4854(31)	0.307(15)	0.307(15)	0.000(0)	-0.307(15)
0.3795(31)	0.307(15)	0.324(16)	0.011(1)	-0.313(16)
0.2839(33)	0.308(16)	0.341(19)	0.022(3)	-0.319(17)
0.2153(35)	0.307(16)	0.351(21)	0.029(4)	-0.322(17)
0.1384(43)	0.307(16)	0.363(24)	0.037(7)	-0.326(19)
0.0939(44)	0.308(17)	0.372(29)	0.043(10)	-0.330(20)

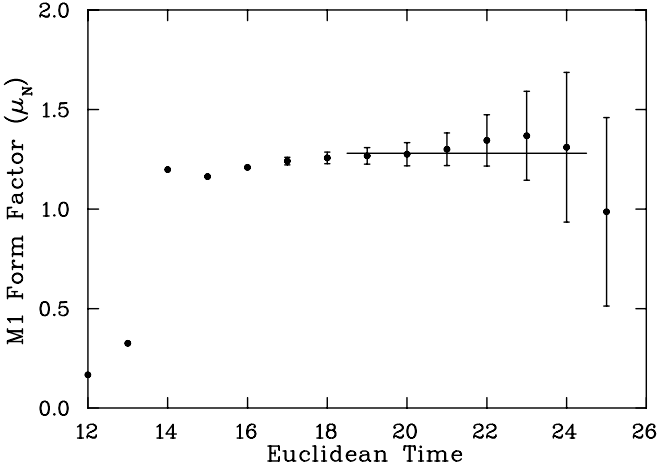


FIG. 5:  $M1$  magnetic form factor of the  $u$  quark in  $\Delta$  at  $Q^2 = 0.230(1)$   $\text{GeV}^2$  as a function of Euclidean time ( $t_2$ ) for  $m_\pi^2 = 0.485(3)$   $\text{GeV}^2$ , the  $SU(3)$ -flavor limit. The line indicates the fitting window and the best fit value.

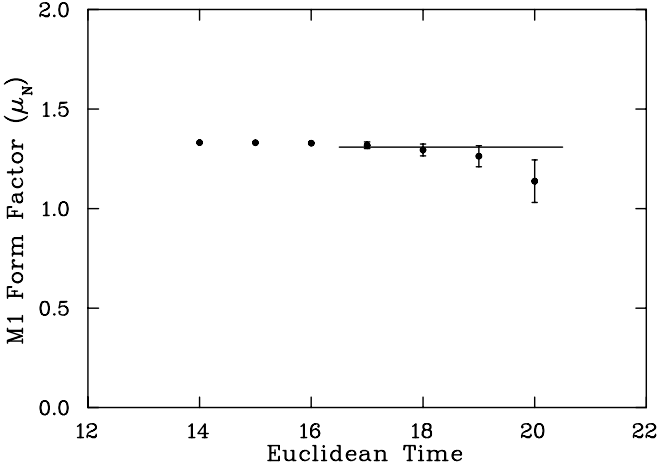


FIG. 6:  $M1$  magnetic form factor of the  $u$  quark in  $\Delta$  at  $Q^2 = 0.230(1)$   $\text{GeV}^2$  at the ninth quark mass where  $m_\pi^2 = 0.215(4)$   $\text{GeV}^2$ . The correlator is obtained from the splitting between the ninth and eighth quark mass results. The line indicates the fitting window and the best fit value.

masses simulated herein. This is supported by experiment where the proton ratio  $\frac{\mathcal{G}_M(Q^2)}{\mu \mathcal{G}_E(Q^2)} \simeq 1$  for values of  $Q^2$  similar to that probed here. In this case

$$\mathcal{G}_M(0) = \frac{\mathcal{G}_M(Q^2)}{\mathcal{G}_E(Q^2)} \mathcal{G}_E(0). \quad (5.5)$$

The strange and light sectors of hyperons will scale differently, and therefore we apply Eq. (5.5) to the individual quark sectors for all the decuplet baryons. Decuplet baryon properties are then reconstructed via

$$\mathcal{G}_M^B(0) = \mathcal{G}_M^l(0) + \mathcal{G}_M^s(0), \quad (5.6)$$

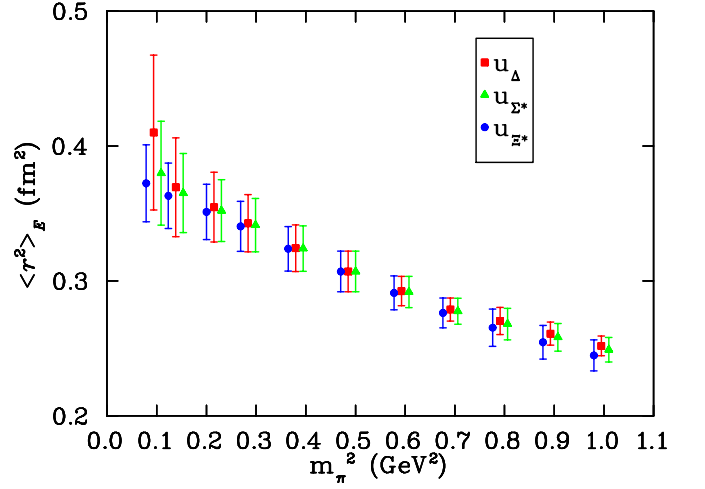


FIG. 7: Charge radii of the  $u$  quark in  $\Delta$ ,  $\Sigma^*$  and  $\Xi^*$  at different quark masses. The values for  $\Delta$  are plotted at  $m_\pi^2$  while that of the  $\Sigma^*$  and  $\Xi^*$  are plotted at shifted  $m_\pi^2$  for clarity.

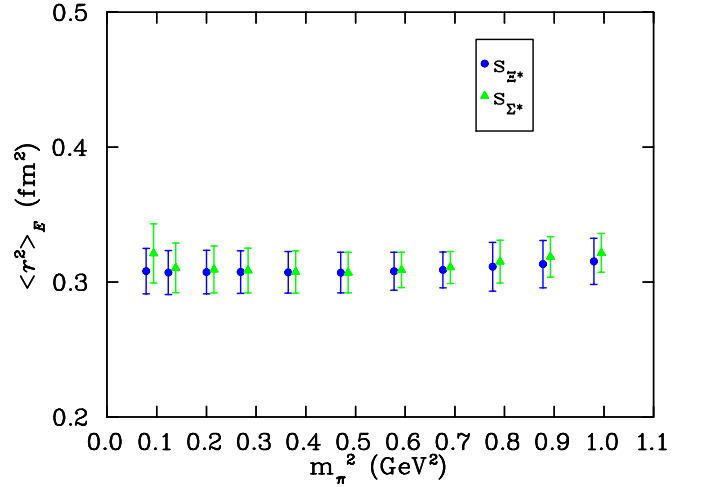


FIG. 8: Charge radii of the  $s$  quark in  $\Sigma^*$  and  $\Xi^*$  at different quark masses. The values for  $\Sigma^*$  are plotted for shifted  $m_\pi^2$  values for clarity.

where  $l$  labels the light quarks and  $s$  labels the strange quark, and quark numbers and charges are included. Similar calculations are performed for the  $u$  and  $d$  sectors of the  $\Delta$ .

In Figs. 17, 18 and 19, we display the quark sector contributions to the decuplet magnetic moments, which are equal in the  $SU(3)_{\text{flavor}}$  limit (sixth quark mass) for single quarks of unit charge. Here we observe that the quark contributions in the  $\Sigma^*$  and  $\Xi^*$  are very similar, which provides evidence that there is little environmental sensitivity. The chiral behavior of the  $u_\Delta$  is also very interesting.

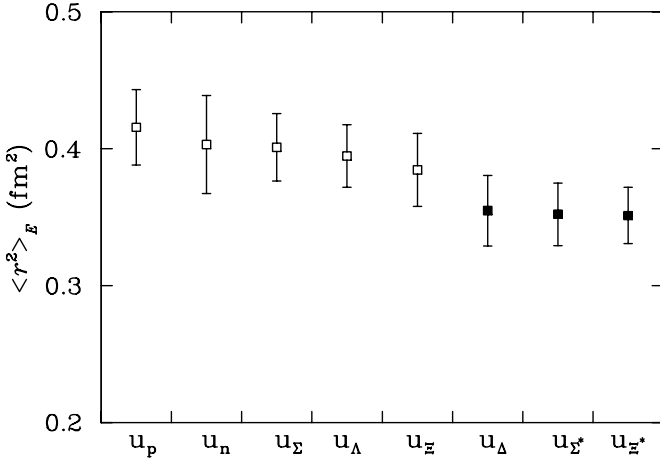


FIG. 9: Charge radii of the  $u$  quark sector in the octet (open squares) and the decuplet (filled squares) baryons at the ninth quark mass where  $m_\pi^2 = 0.215(4)$  GeV $^2$ .

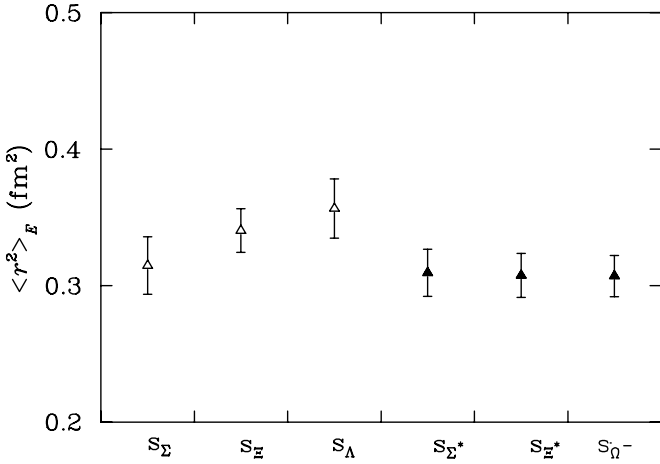


FIG. 10: Charge radii of the  $s$  quark sector in the octet (open squares) and the decuplet (filled squares) baryons at the ninth quark mass where  $m_\pi^2 = 0.215(4)$  GeV $^2$ .

### C. Effective Moments

In order to compare the decuplet moments with the octet moments from our previous lattice calculation [14], we construct so-called effective moments by equating the lattice quark sector contributions to the same sector of the SU(6)-magnetic moment formula derived from SU(6)-spin-flavor symmetry wave functions.

The simple quark model formula from SU(6)-spin-flavor symmetry gives the magnetic moment of the proton as

$$\mu_p = \frac{4}{3}\mu_u - \frac{1}{3}\mu_d, \quad (5.7)$$

where  $\mu_u$  and  $\mu_d$  are the intrinsic magnetic moments of the doubly represented  $u$  and singly represented  $d$  con-

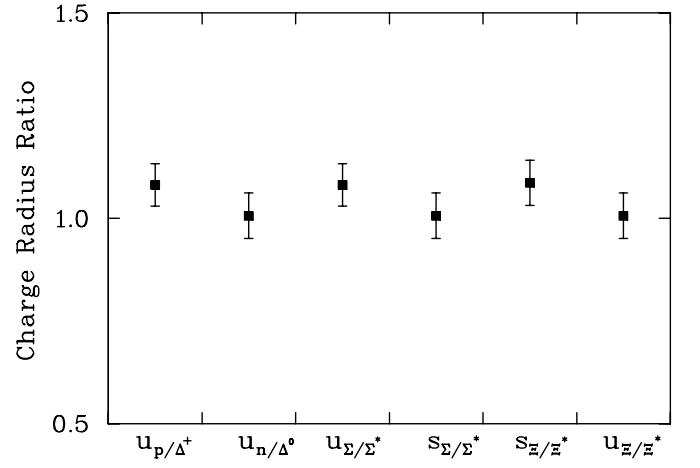


FIG. 11: Ratio of charge radii of the quark sector contributions in the octet/decuplet baryons at the  $SU(3)_{\text{flavor}}$  limit where  $m_\pi^2 = 0.485(3)$  GeV $^2$ .

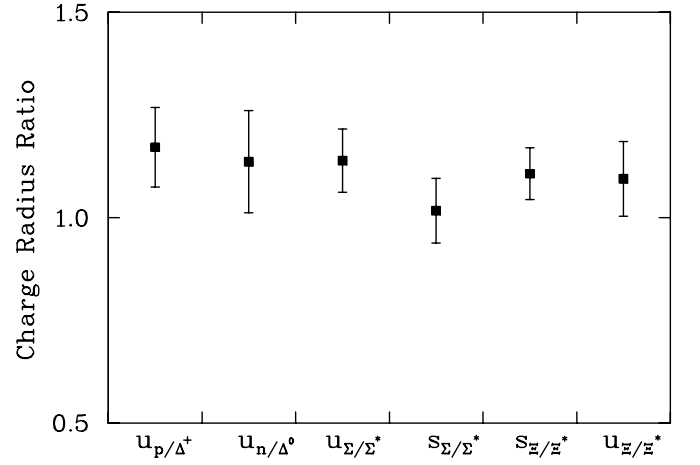


FIG. 12: Ratio of charge radii of the quark sector contributions in the octet/decuplet baryons at the ninth quark mass where  $m_\pi^2 = 0.215(4)$  GeV $^2$ .

stituent quarks, respectively, per single quark. This can be generalized for any baryon with two doubly represented quarks  $D$  and one singly represented quark  $S$ . Focusing on the proton and using the charge factors of the doubly represented and singly represented quarks as  $2/3$  and  $(-1/3)$  respectively, we define effective moments for single quarks of unit charge,  $\mu^{\text{Eff}}$ , by

$$\mu_u = \frac{2}{3}\mu_D^{\text{Eff}}, \quad \mu_d = -\frac{1}{3}\mu_S^{\text{Eff}}, \quad (5.8)$$

such that Eq. (5.7) becomes

$$\mu_p = \left(\frac{4}{3}\right) \left(\frac{2}{3}\right) \mu_D^{\text{Eff}} - \left(\frac{1}{3}\right) \left(-\frac{1}{3}\right) \mu_S^{\text{Eff}}, \quad (5.9)$$

where the charge factors within  $\mu_u$  and  $\mu_d$  are now explicit.

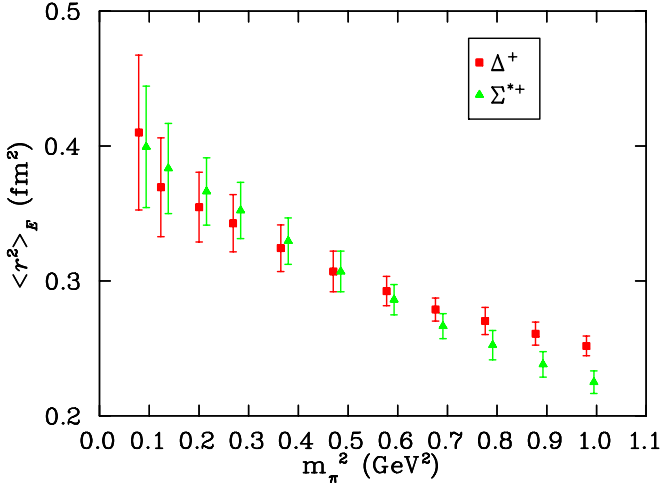


FIG. 13: Charge radii of  $\Delta^+$  and  $\Sigma^{*+}$  at different quark masses. The values for  $\Sigma^*$  are plotted at shifted  $m_\pi^2$  for clarity.

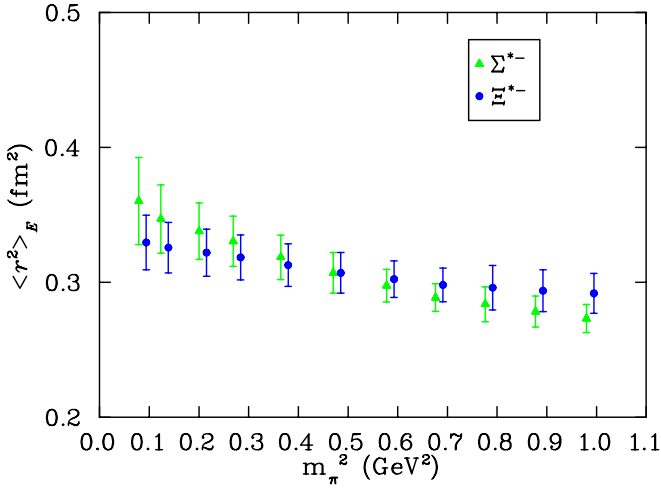


FIG. 14: Charge radii (magnitude) of  $\Sigma^{*-}$  and  $\Xi^{*-}$  at different quark masses. The values for  $\Xi^{*-}$  are plotted at shifted  $m_\pi^2$  for clarity.

On the lattice we calculate the baryon magnetic moments from the individual quark sector contributions using

$$\mu_p = 2 \left( \frac{2}{3} \right) \mu_D^{\text{Latt}} + 1 \left( -\frac{1}{3} \right) \mu_S^{\text{Latt}}. \quad (5.10)$$

In the above equation the factors 2 and 1 in the first and second term account for the number of doubly and singly represented quarks, while the charges are indicated in parentheses. Equating quark sectors in Eqs. (5.9) and (5.10) yields for the effective moments,

$$\begin{aligned} \mu_S^{\text{Eff}} &= -3\mu_S^{\text{Latt}}, \\ \mu_D^{\text{Eff}} &= \frac{3}{2}\mu_D^{\text{Latt}}. \end{aligned} \quad (5.11)$$

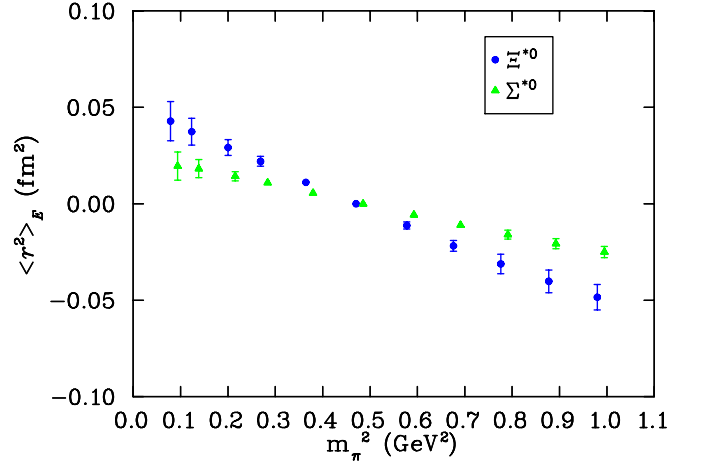


FIG. 15: Charge radii of  $\Sigma^{*0}$  and  $\Xi^{*0}$  at different quark masses. The values for  $\Sigma^{*0}$  are plotted at shifted  $m_\pi^2$  for clarity.

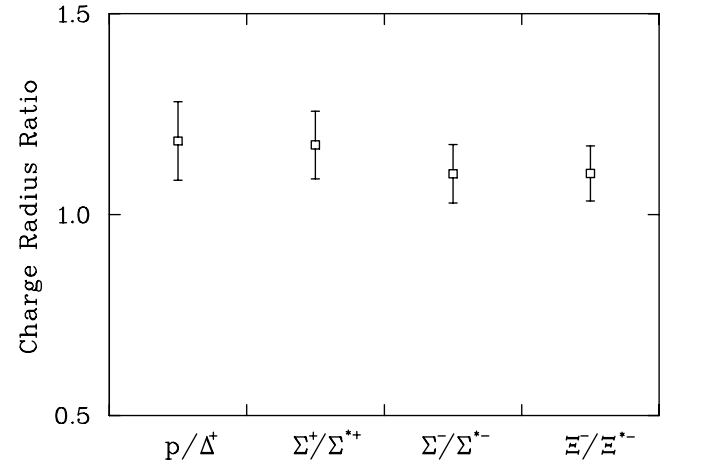


FIG. 16: Ratio of charge radii of the octet/decuplet baryons at the ninth quark mass where  $m_\pi^2 = 0.215(4)$  GeV<sup>2</sup>.

One could also define a constituent quark mass via

$$\begin{aligned} \mu_S^{\text{Eff}} &= \frac{e}{2m_S^{\text{Eff}}}, \\ \mu_D^{\text{Eff}} &= \frac{e}{2m_D^{\text{Eff}}}, \end{aligned} \quad (5.12)$$

revealing that  $\mu_S^{\text{Eff}} \simeq \mu_D^{\text{Eff}}$  in most constituent quark models.

For the decuplet baryons, the magnetic moment is the sum of the individual constituent-quark contributions. Hence Eq. (5.9) for the  $\Delta$  baryons becomes

$$\mu_{\Delta^+} = 2 \left( \frac{2}{3} \right) \mu_D^{\text{Eff}} + 1 \left( -\frac{1}{3} \right) \mu_S^{\text{Eff}}. \quad (5.13)$$

On the lattice this is exactly the equation we use to build the decuplet baryon moments from the quark sector contributions. Therefore, the quark level magnetic moments



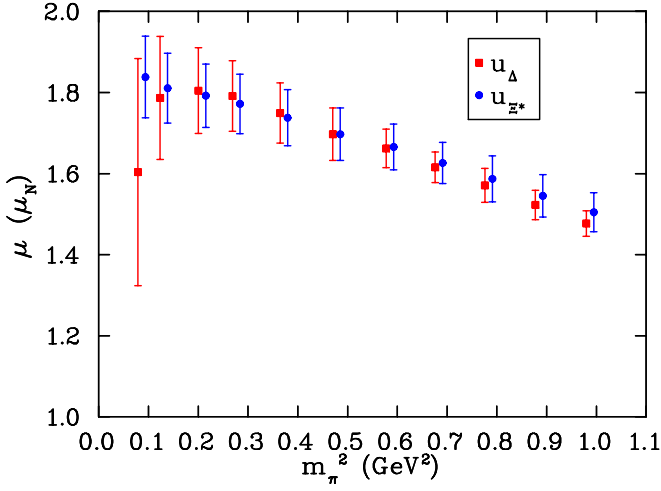


FIG. 17: Magnetic moments of a  $u$  quark in  $\Delta$  and  $\Xi^*$  as a function of quark mass. The values for  $\Xi^*$  are plotted at shifted  $m_\pi^2$  for clarity.

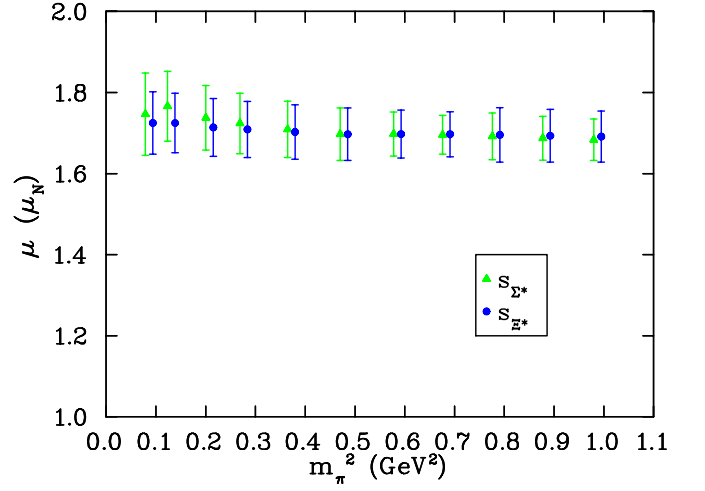


FIG. 19: Magnetic moments of an  $s$  quark in  $\Sigma^*$  and  $\Xi^*$  for different quark masses. The values for  $\Xi^*$  are plotted at shifted  $m_\pi^2$  for clarity.

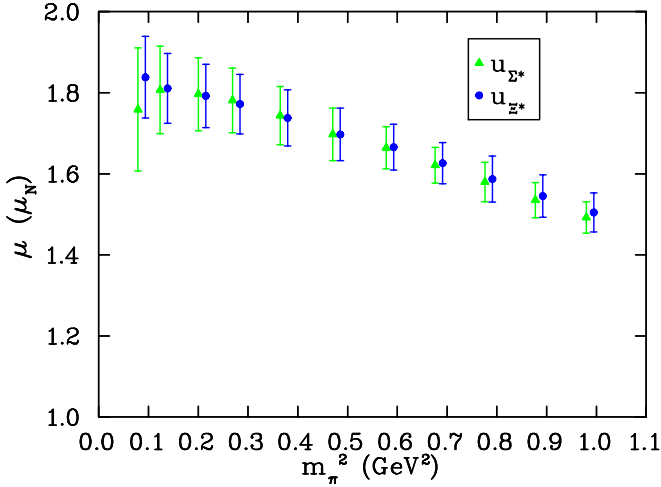


FIG. 18: Magnetic moments of a  $u$  quark in  $\Sigma^*$  and  $\Xi^*$  as a function of quark mass. The values for  $\Xi^*$  are plotted at shifted  $m_\pi^2$  for clarity.

that we calculate are the effective moments of the quarks for both the doubly and singly represented quarks, *i.e.*,

$$\mu^{\text{Eff}} = \mu^{\text{Latt}}. \quad (5.14)$$

In Figs. 20 and 21 we plot the effective moments of the  $u$  and  $s$  quark sectors of the octet and decuplet baryons at the ninth quark mass. Here we observe that the quarks in the octet baryons show far more environmental sensitivity than their counterparts in the decuplet baryons.

The baryon magnetic moments are plotted in Figs. 22, 23 and 24. For the magnetic moment of  $\Omega^-$  we take the value of  $\mu_{\Delta^-}$  at the SU(3) limit *viz.*,  $-1.697 \pm 0.065 \mu_N$ , which is smaller than the value given by the Particle Data Group ( $-2.02 \pm 0.05 \mu_N$ ).

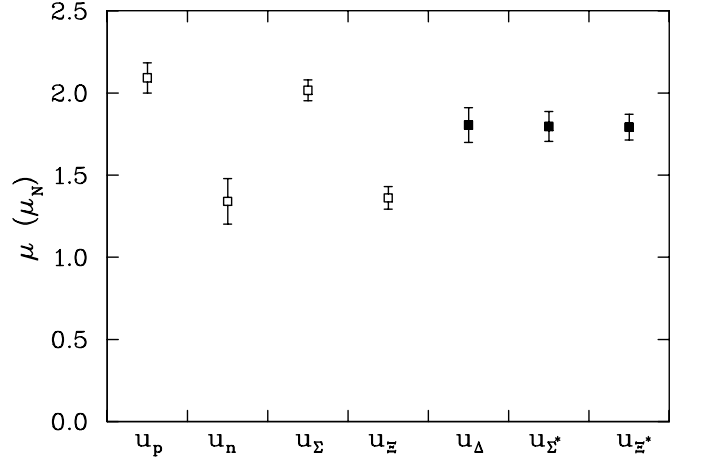


FIG. 20: Effective moments of the  $u$  quark sector in the octet and the decuplet baryons at the ninth quark mass where  $m_\pi^2 = 0.215(4) \text{ GeV}^2$ .

This discrepancy could be partly due to the fact that the mass of  $\Omega^-$  from our lattice calculation ( $1.73 \pm 0.012 \text{ GeV}$ ) is slightly larger than the experimentally measured value ( $1.67 \text{ GeV}$ ).

Another reason for this discrepancy is likely to reside in the absence of  $K\Xi$  loops in the virtual decay of  $\Omega^-$ . The virtual transition  $\Omega \rightarrow \Xi K$  requires the presence of a light sea-quark flavor, while in QQCD, there is only a heavy valence strange quark. In reality this would provide an important contribution, since  $\Xi$  is a lower mass state than  $\Omega^-$ . The predominant contribution is  $\Omega^0 \rightarrow \Xi^0 K^-$  with the  $z$ -component of angular momentum in the positive direction. This process will act to enhance the magnitude of the negative moment. The absence of such loops in QQCD represents missing physics and causes the dis-

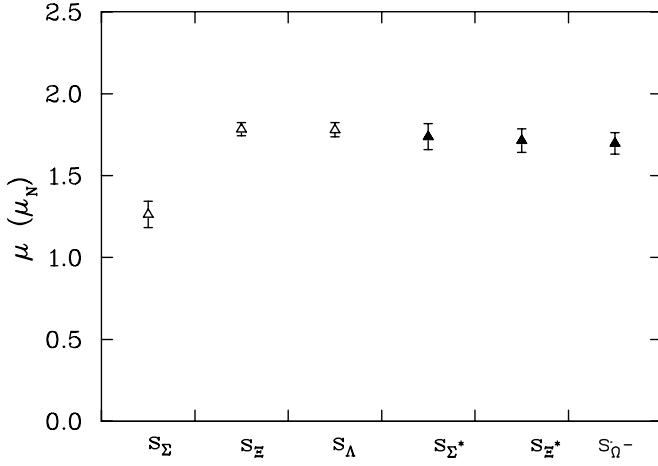


FIG. 21: Effective moments of the  $s$  quark sector in the octet and the decuplet baryons at the ninth quark mass where  $m_\pi^2 = 0.215(4)$   $\text{GeV}^2$ .

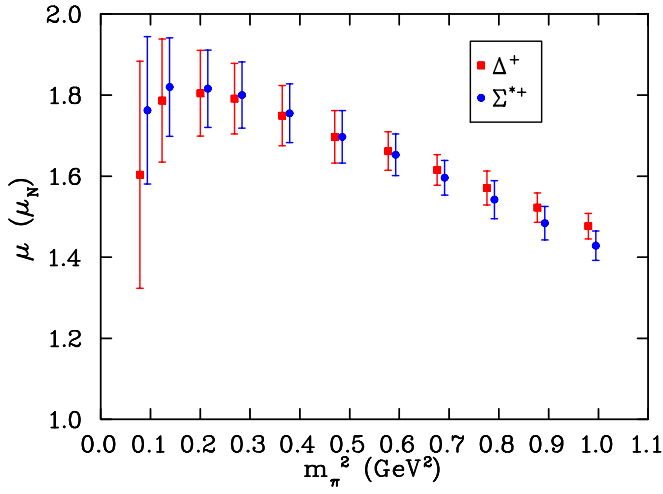


FIG. 22: Magnetic moments of  $\Delta^+$  and  $\Sigma^{*+}$  at different quark masses. The values for  $\Sigma^{*+}$  are plotted at shifted  $m_\pi^2$  for clarity.

crepancy from the values of full QCD. This is certainly a good place to search for dynamical sea quark effects.

Figure 25 compares the magnetic moment of the  $\Delta^+$  with our earlier result for the proton magnetic moment on the same set of gauge field configurations [14]. A simple quark model predicts that the proton and the  $\Delta^+$  have equal magnetic moments. However the interplay between the different pion-loop contributions to the  $\Delta^+$  magnetic moments indicate that the proton magnetic moment should be greater than that of the  $\Delta^+$  in Full QCD [36].

The presence of the  $\Delta \rightarrow N\pi$  decay channel is particularly important for the quark mass dependence of  $\Delta$  properties [37]. Rapid curvature associated with non-analytic behavior is shifted to larger pion masses near

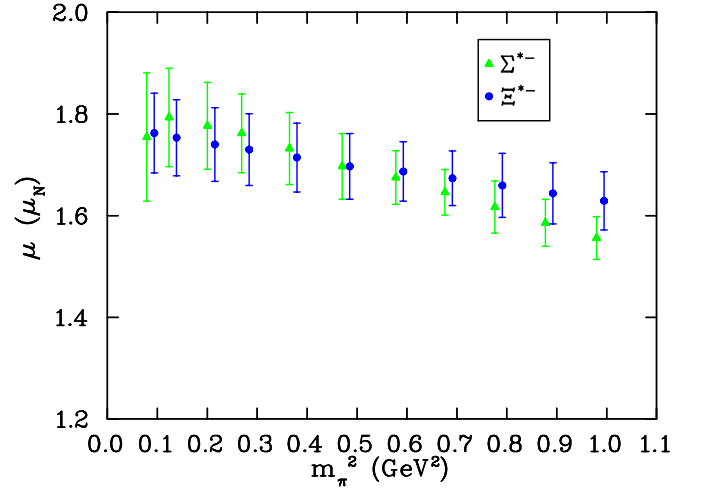


FIG. 23: Magnetic moments (magnitude) of  $\Sigma^{*-}$  and  $\Xi^{*-}$  at different quark masses. The values for  $\Xi^{*-}$  are plotted at shifted  $m_\pi^2$  for clarity.

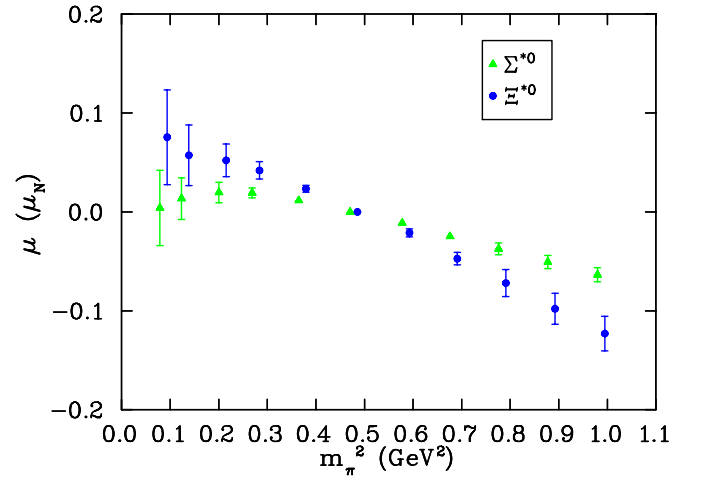


FIG. 24: Magnetic moments of  $\Sigma^{*0}$  and  $\Xi^{*0}$  at different quark masses. The values for  $\Xi^{*0}$  are plotted at shifted  $m_\pi^2$  for clarity.

the  $N$ - $\Delta$  mass splitting,  $m_\pi \sim M_\Delta - M_N$ . As described below, quenched-QCD decay-channel contributions come with a sign opposite to that of full QCD. This artifact holds tremendous promise for revealing unmistakable signatures of the quenched meson cloud.

The change in sign for the decay-channel contributions is easily understood through the consideration of the quark flow diagrams in Fig. 26, illustrating the meson-cloud contributions to the  $\Delta^{++}$  resonance in full QCD. Quark flow diagram (a) corresponds to the hadronic process described in the top left diagram of Fig. 26. Since QCD is flavor-blind, the process illustrated in diagram (b) is equivalent to diagram (a) provided the masses of the  $u$  and  $d$  quarks are taken to be equal. On its own, diagram (b) describes the decay of the  $\Delta^{++}$  to a doubly-

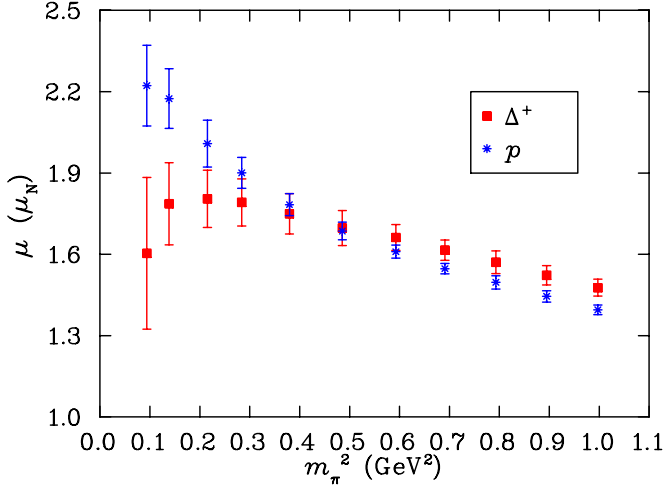


FIG. 25: Magnetic moments of  $\Delta^+$  and the proton at different quark masses.

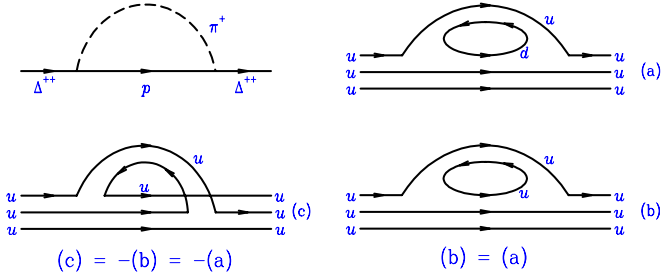


FIG. 26: Quark-flow diagrams for meson-cloud contributions to  $\Delta^{++}$  in full QCD.

charged  $uuu$  “proton,” which we denote  $p^{++}$ . Of course, such states do not exist in full QCD and diagram (c) provides a contribution which is exactly equal but opposite in sign to diagram (b) when the intermediate state is a  $uuu$  proton. Upon quenching the theory, both diagrams (a) and (b) are eliminated, leaving only diagram (c). Hence the physics of the  $\Delta \rightarrow N\pi$  decay is present in the quenched approximation [32] but its contribution has the wrong sign. This signature of quenched chiral physics is manifest in our results.

All the decuplet baryons show, to some extent, a turn over of the magnetic moment in the low quark mass region just above the opening of the  $N\pi$  decay channel. The magnitude of the turn over is dampened by the presence of a strange quark, which is seen by the fact that  $\Sigma^*$  has a smaller turn over than  $\Delta$ . The  $\Xi$  baryons with two  $s$  quarks only admit Kaon loops and do not display a turn over, further clarifying a link to chiral physics.

Magnetic moments of the decuplet baryons are listed in Tables XIII to XV.

TABLE XIII: Magnetic moments of the  $\Delta^+$  in nuclear magnetons for different  $m_\pi^2$  in  $\text{GeV}^2$ . Quark sector contributions for single quarks of unit charge are also provided. The magnetic moment of  $\Delta^-$  is equal in magnitude to that of  $\Delta^+$  with a negative sign and that of  $\Delta^0$  is 0. Charge symmetry also requires that the  $\Delta^{++}$  has a magnetic moment twice that of  $\Delta^+$ . The magnetic moment of  $\Omega^-$  is that of  $\Delta^-$  at the  $SU(3)_{\text{flavor}}$  limit where  $m_\pi^2 = 0.4854(31) \text{ GeV}^2$ , and takes the value  $-1.697(65) \mu_N$ .

$m_\pi^2$	$u_\Delta (\mu_N)$	$d_\Delta (\mu_N)$	$\Delta^+ (\mu_N)$
0.9960(56)	1.466(31)	1.466(31)	1.466(31)
0.8936(56)	1.512(36)	1.512(36)	1.512(36)
0.7920(55)	1.559(42)	1.559(42)	1.559(42)
0.6920(54)	1.604(50)	1.604(50)	1.604(50)
0.6910(35)	1.615(38)	1.615(38)	1.615(38)
0.5925(33)	1.662(48)	1.662(48)	1.662(48)
0.4854(31)	1.697(65)	1.697(65)	1.697(65)
0.3795(31)	1.749(74)	1.749(74)	1.749(74)
0.2839(33)	1.792(87)	1.792(87)	1.792(87)
0.2153(35)	1.80(11)	1.80(11)	1.80(11)
0.1384(43)	1.79(15)	1.79(15)	1.79(15)
0.0939(44)	1.60(28)	1.60(28)	1.60(28)

TABLE XIV: Magnetic moments of  $\Sigma^*$ ,  $\Sigma^{*0}$  and  $\Sigma^{*-}$  in nuclear magnetons with quark sector contributions for a single quark of unit charge at different  $m_\pi^2$  values.

$m_\pi^2$	$u_{\Sigma^*} (\mu_N)$	$s_{\Sigma^*} (\mu_N)$	$\Sigma^{*+} (\mu_N)$	$\Sigma^{*0} (\mu_N)$	$\Sigma^{*-} (\mu_N)$
0.9960(56)	1.482(38)	1.671(51)	1.418(36)	-0.063(7)	-1.545(42)
0.8936(56)	1.524(43)	1.675(54)	1.474(41)	-0.050(7)	-1.574(46)
0.7920(55)	1.568(48)	1.680(57)	1.531(47)	-0.037(6)	-1.605(51)
0.6920(54)	1.609(55)	1.683(62)	1.585(54)	-0.025(5)	-1.634(57)
0.6910(35)	1.621(44)	1.696(48)	1.596(43)	-0.025(3)	-1.646(45)
0.5925(33)	1.664(52)	1.698(54)	1.653(51)	-0.011(2)	-1.675(53)
0.4854(31)	1.697(65)	1.697(65)	1.697(65)	0.000(0)	-1.697(65)
0.3795(31)	1.744(72)	1.709(69)	1.755(72)	0.012(2)	-1.732(71)
0.2839(33)	1.781(80)	1.724(75)	1.800(82)	0.019(5)	-1.762(78)
0.2153(35)	1.796(90)	1.738(80)	1.816(95)	0.020(10)	-1.777(85)
0.1384(43)	1.81(11)	1.766(86)	1.82(12)	0.013(21)	-1.793(97)
0.0939(44)	1.76(15)	1.75(10)	1.76(18)	0.004(38)	-1.75(13)

TABLE XV: Magnetic moments of  $\Xi^{*0}$  and  $\Xi^{*-}$  in nuclear magnetons with quark sector contributions for a single quark of unit charge at different  $m_\pi^2$  values.

$m_\pi^2$	$s_{\Xi^*} (\mu_N)$	$u_{\Xi^*} (\mu_N)$	$\Xi^{*0} (\mu_N)$	$\Xi^{*-} (\mu_N)$
0.9960(56)	1.681(63)	1.494(48)	-0.124(18)	-1.619(57)
0.8936(56)	1.683(65)	1.534(52)	-0.099(16)	-1.633(60)
0.7920(55)	1.685(67)	1.576(56)	-0.073(14)	-1.649(63)
0.6920(54)	1.687(69)	1.615(62)	-0.048(11)	-1.663(67)
0.6910(35)	1.697(56)	1.626(51)	-0.047(6)	-1.674(54)
0.5925(33)	1.698(59)	1.666(57)	-0.021(4)	-1.687(58)
0.4854(31)	1.697(65)	1.697(65)	0.000(0)	-1.697(65)
0.3795(31)	1.703(67)	1.738(69)	0.023(4)	-1.714(68)
0.2839(33)	1.709(69)	1.772(73)	0.042(9)	-1.730(70)
0.2153(35)	1.714(71)	1.792(78)	0.052(16)	-1.740(73)
0.1384(43)	1.725(73)	1.811(86)	0.057(31)	-1.753(75)
0.0939(44)	1.725(77)	1.84(10)	0.076(48)	-1.763(79)

### D. Electric Quadrupole Form Factors

The  $E2$  form factors of the spin-3/2 decuplet baryons provide interesting information about the distribution of charge and its deviation from spherical symmetry. In Fig. 27 we show the correlation function proportional to the  $E2$  quadrupole form factor of the  $u$  quark in  $\Delta$  at the  $SU(3)_{\text{flavor}}$  limit, in units of  $e/M_N^2$ , as a function of Euclidean time. Figure 28 indicates the quadrupole form factor of the  $u$  quark in  $\Delta$  at the ninth quark mass. Here the employment of the splittings technique facilitates the extraction of the signal. In both cases a nontrivial result is obtained. As mentioned in Sec. IID, we consider the symmetry of the last two terms in Eq. (2.35) as the deciding factor in selecting the upper limit of the fit-window.

The quark sector contributions to the form factors in units of  $e/M_N^2$  of all the decuplet members are indicated in Tables XVI to XVIII. For an axially deformed object the quadrupole form factor is related to the charge distribution in the Breit frame through [7]

$$\mathcal{G}_{E2}(0) = M_B^2 \int d^3 r \bar{\psi}(r) (3z^2 - r^2) \psi(r), \quad (5.15)$$

where  $3z^2 - r^2$  is the standard operator used for quadrupole moments. A positive quadrupole form factor for a positively charged baryon indicates a prolate charge distribution, while a negative quadrupole form factor indicates an oblate charge distribution. In non-relativistic models, the  $E2$  form factor vanishes unless some configuration mixing of higher orbital-angular momentum states is included in the baryon ground state.

The  $E2$  form factors of the charged decuplet baryons in units of  $\text{fm}^2$  for different values of  $m_\pi^2$  are listed in table XIX. The  $E2$  form factor of the  $\Delta^0$  is identically equal to zero and for the other neutral baryons, it is close to zero. The results for the charged decuplet baryons are non-zero, indicating that they have a deformed shape.

The quark sector contributions to the  $E2$  form factors are shown in Figs. 29 to 31. Once again, the importance of chiral physics is manifest in these results. A significant enhancement of the magnitude of the light-quark sector contribution to the  $E2$  form factor is observed in the  $\Delta$  as the opening of the  $N\pi$  decay channel is approached. A similar effect is seen, to a lesser extent, in the  $\Sigma^*$ , while for the  $\Xi^-$  no chiral curvature is observed due to the two  $s$  quarks admitting only Kaon loops, as discussed in the previous section. The  $E2$  form factors for the various decuplet baryons are shown in Figs. 32 to 34.

From our simulation we conclude that the  $E2$  form factor of the  $\Omega^-$  baryon (the value of the  $\Delta^-$  form factor at  $SU(3)_{\text{flavor}}$  limit) is  $(0.86 \pm 0.12) \times 10^{-2} \text{ fm}^2$ . The accuracy of our result indicates a definite non-zero value of the  $E2$  form factor of  $\Omega^-$ , and we favor a positive value. Since  $\Omega^-$  is a negatively charged baryon, this result implies that it has an oblate shape, with the equatorial axis being larger than the polar axis.

Similarly the  $E2$  form factor for the  $\Delta^+$  is  $(-0.86 \pm 0.12) \times 10^{-2} \text{ fm}^2$  at the  $SU(3)$  flavor symmetry point.

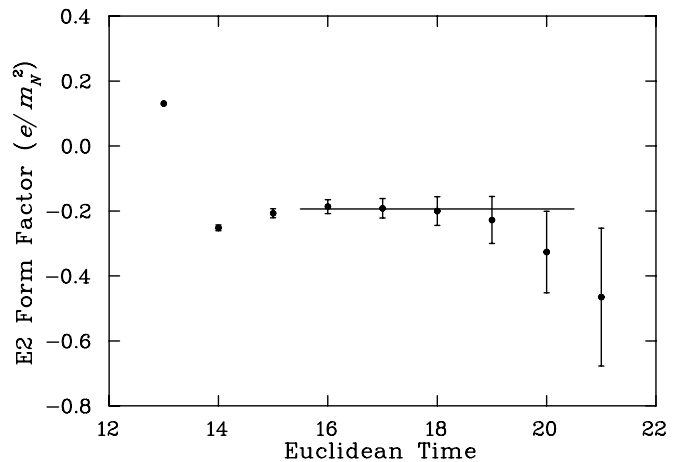


FIG. 27:  $E2$  electric form factor of the  $u$  or  $d$  quark sector of the  $\Delta$  at the  $SU(3)_{\text{flavor}}$  limit as a function of time.

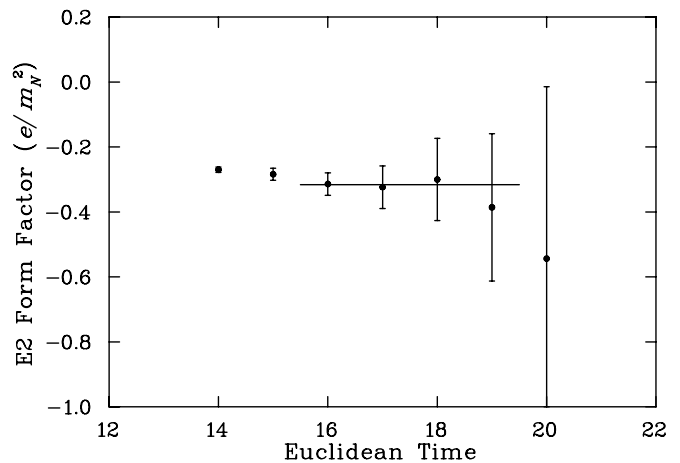


FIG. 28:  $E2$  electric form factor of the  $u$  or  $d$  quark sector of the  $\Delta$  as a function of time at the ninth quark mass where  $m_\pi^2 = 0.215(4) \text{ GeV}^2$ .

Our results for the  $\Delta^+$  compare favorably with the results of Ref. [8]. Using the closest available pion masses of 533(3) MeV, and 563(4) MeV for this study, and [8] respectively, we find the  $E2$  form factor to be  $(-1.16 \pm 29) \times 10^{-2} \text{ fm}^2$ , to be compared with  $(-1.08 \pm 40) \times 10^{-2} \text{ fm}^2$ . We note however, that this study is performed at a finite  $Q^2 = 0.230(1) \text{ GeV}^2$ , whilst [8] reports results at  $Q^2 = 0$ .

The negative  $E2$  form factor of a positive  $\Delta^+$  baryon implies an oblate shape in the Breit frame. As illustrated in Fig. 32, the  $E2$  form factor grows substantially in magnitude as the chiral limit is approached, taking the value  $-0.030(11) \text{ fm}^2$  at our lightest quark mass. We note that the  $E2$  form factor of  $\Delta^{++}$  is twice that of the  $\Delta^+$   $E2$  form factor and hence takes the value  $-0.060(23) \text{ fm}^2$  at our lightest quark mass.

TABLE XVI: Quark sector contributions to the  $E2$  form factor of  $\Delta$  at  $Q^2 = 0.230(1)$  GeV<sup>2</sup> in fixed units of  $e/m_N^2$ . Sector contributions are for a single quark having unit charge. The fit windows are selected using the criteria outlined in Ref. [14].

$m_\pi^2$ (GeV <sup>2</sup> )	$u_\Delta$			$d_\Delta$		
	fit value	fit window	$\chi_{\text{dof}}^2$	fit value	fit window	$\chi_{\text{dof}}^2$
0.9960(56)	-0.117(16)	16 – 20	1.63	-0.117(16)	16 – 20	1.63
0.8936(56)	-0.123(18)	16 – 20	1.39	-0.123(18)	16 – 20	1.39
0.7920(55)	-0.130(22)	16 – 20	1.16	-0.130(22)	16 – 20	1.16
0.6920(54)	-0.137(26)	16 – 20	1.01	-0.137(26)	16 – 20	1.01
0.6910(35)	-0.163(17)	16 – 20	0.76	-0.163(17)	16 – 20	0.76
0.5925(33)	-0.177(21)	16 – 20	0.75	-0.177(21)	16 – 20	0.75
0.4854(31)	-0.194(27)	16 – 20	0.86	-0.194(27)	16 – 20	0.86
0.3795(31)	-0.218(40)	16 – 19	1.03	-0.218(40)	16 – 19	1.03
0.2839(33)	-0.263(67)	16 – 19	1.57	-0.263(67)	16 – 19	1.57
0.2153(35)	-0.32(11)	16 – 19	1.20	-0.32(11)	16 – 19	1.20
0.1384(43)	-0.52(20)	16 – 18	0.72	-0.52(20)	16 – 18	0.72
0.0939(44)	-0.68(26)	15 – 16	1.06	-0.68(26)	15 – 16	1.06

TABLE XVII: Quark sector contributions to the  $E2$  form factor of  $\Sigma^*$  at  $Q^2 = 0.230(1)$  GeV<sup>2</sup> in units of  $e/m_N^2$ . Sector contributions are for a single quark having unit charge. The fit windows are selected using the criteria outlined in Ref. [14].

$m_\pi^2$ (GeV <sup>2</sup> )	$u_{\Sigma^*}$ or $d_{\Sigma^*}$			$s_{\Sigma^*}$		
	fit value	fit window	$\chi_{\text{dof}}^2$	fit value	fit window	$\chi_{\text{dof}}^2$
0.9960(56)	-0.132(19)	16 – 20	1.52	-0.113(29)	16 – 20	0.75
0.8936(56)	-0.136(22)	16 – 20	1.36	-0.118(31)	16 – 20	0.71
0.7920(55)	-0.145(25)	16 – 20	1.20	-0.124(33)	16 – 20	0.66
0.6920(54)	-0.147(29)	16 – 20	1.07	-0.131(36)	16 – 20	0.65
0.6910(35)	-0.172(18)	16 – 20	0.91	-0.170(22)	16 – 20	0.48
0.5925(33)	-0.183(22)	16 – 20	0.89	-0.180(24)	16 – 20	0.61
0.4854(31)	-0.194(27)	16 – 20	0.86	-0.194(27)	16 – 20	0.86
0.3795(31)	-0.208(36)	16 – 20	0.48	-0.211(32)	16 – 20	1.89
0.2839(33)	-0.225(51)	16 – 17	0.41	-0.231(38)	16 – 17	0.61
0.2153(35)	-0.233(73)	16 – 19	1.08	-0.257(48)	16 – 19	1.84
0.1384(43)	-0.29(11)	16 – 17	1.71	-0.300(67)	16 – 17	1.07
0.0939(44)	-0.42(16)	16 – 17	0.94	-0.325(88)	16 – 17	0.31

### E. Magnetic Octupole Moments

The magnetic octupole form factors are calculated on the lattice by considering a combination of ratios of three and two-point functions as given in Eq. (2.32).

Figure 35 provides a plot of the correlator proportional to the  $M3$  form factor of a  $u$  quark in the  $\Delta$  as a function of Euclidean time at the  $SU(3)$  flavor limit. Figure 36 provides the  $M3$  form factor at the ninth quark mass, where a plateau is realized using the splittings method. Tables XX to XXII list the quark sector  $M3$  form factors. The magnetic octupole form factors ( $M3$ ) of the decuplet baryons are listed in Table XXIII.

Plots of the quark sector contributions to the  $M3$  form factors are provided in Figs. 37 to 39. Figs. 40 to 42 show

the  $M3$  form factors for the decuplet baryons.

Like  $E2$ , the  $M3$  form factors require nonzero orbital angular momentum admixtures in the ground state wave function [7]. Our statistics are sufficient to reveal a non-trivial result for the  $M3$  form factor of the  $\Delta$  for the first time. We find a result of  $-3.7(3.3) e/2m_N^3$  for the  $\Delta^+$  at a squared pion mass of  $0.094(4)$  GeV<sup>2</sup>, close to the physical limit. At larger masses the results are consistent with zero, but systematically negative, with enhancement at the lightest masses for the  $\Delta$ , and to a lesser extent the  $\Sigma^*$ .

TABLE XVIII: Quark sector contributions to the  $E2$  form factor of  $\Xi^*$  at  $Q^2 = 0.230(1)$  GeV<sup>2</sup> in units of  $e/m_N^2$ . Sector contributions are for a single quark having unit charge. The fit windows are selected using the criteria outlined in Ref. [14].

$m_\pi^2$ (GeV <sup>2</sup> )	$s_{\Xi^*}$			$u_{\Xi^*}$ or $d_{\Xi^*}$		
	fit value	fit window	$\chi_{\text{dof}}^2$	fit value	fit window	$\chi_{\text{dof}}^2$
0.9960(56)	-0.127(36)	16 – 20	0.64	-0.157(25)	16 – 20	1.75
0.8936(56)	-0.131(37)	16 – 20	0.64	-0.157(27)	16 – 20	1.52
0.7920(55)	-0.136(39)	16 – 20	0.64	-0.159(30)	16 – 20	1.35
0.6920(54)	-0.141(40)	16 – 20	0.66	-0.159(33)	16 – 20	1.18
0.6910(35)	-0.180(24)	16 – 20	0.65	-0.184(20)	16 – 20	1.17
0.5925(33)	-0.186(25)	16 – 20	0.73	-0.190(23)	16 – 20	1.04
0.4854(31)	-0.194(27)	16 – 20	0.86	-0.194(27)	16 – 20	0.86
0.3795(31)	-0.201(29)	16 – 17	0.82	-0.198(33)	16 – 21	0.62
0.2839(33)	-0.208(31)	16 – 17	0.59	-0.200(41)	16 – 17	0.23
0.2153(35)	-0.214(34)	16 – 17	0.80	-0.191(52)	16 – 17	0.06
0.1384(43)	-0.222(38)	16 – 17	0.92	-0.184(71)	16 – 18	0.34
0.0939(44)	-0.222(41)	15 – 16	0.17	-0.183(82)	15 – 16	0.70

TABLE XIX:  $E2$  form factors at  $Q^2 = 0.230(1)$  GeV<sup>2</sup> of the charged decuplet baryons in units of  $10^{-2}\text{fm}^2$  for different  $m_\pi^2$  values. The  $E2$  form factor of the  $\Delta^-$  at the  $SU(3)_{\text{flavor}}$  limit where  $m_\pi^2 = 0.485(3)$  provides the  $E2$  form factor of  $\Omega^-$ .

$m_\pi^2$ (GeV <sup>2</sup> )	$\Delta^{++}$	$\Delta^+$	$\Delta^-$	$\Sigma^{*+}$	$\Sigma^{*-}$	$\Xi^{*-}$
0.9972(55)	-1.03(14)	-0.517(69)	0.517(69)	-0.613(77)	0.555(97)	0.60(14)
0.8936(56)	-1.08(16)	-0.541(80)	0.541(80)	-0.629(88)	0.57(11)	0.62(15)
0.7920(55)	-1.15(19)	-0.575(96)	0.575(96)	-0.65(10)	0.60(12)	0.63(16)
0.6920(54)	-1.21(23)	-0.61(12)	0.61(12)	-0.67(12)	0.63(14)	0.65(17)
0.6910(35)	-1.44(15)	-0.718(75)	0.718(75)	-0.765(77)	0.757(86)	0.80(10)
0.5925(33)	-1.56(18)	-0.782(91)	0.782(91)	-0.813(92)	0.804(99)	0.83(11)
0.4854(31)	-1.71(24)	-0.86(12)	0.86(12)	-0.86(12)	0.86(12)	0.86(12)
0.3795(31)	-1.93(35)	-0.96(18)	0.96(18)	-0.91(17)	0.92(15)	0.88(13)
0.2839(33)	-2.32(59)	-1.16(29)	1.16(29)	-0.99(25)	1.00(20)	0.91(15)
0.2153(35)	-2.79(95)	-1.40(48)	1.40(48)	-0.99(37)	1.07(28)	0.91(17)
0.1384(43)	-4.6(1.8)	-2.31(88)	2.31(88)	-1.28(58)	1.30(41)	0.92(21)
0.0939(44)	-6.0(2.3)	-3.0(1.1)	3.0(1.1)	-1.99(86)	1.71(57)	0.92(23)

TABLE XX: Quark sector contributions to the  $M3$  form factor of  $\Delta$  at  $Q^2 = 0.230(1)$  GeV<sup>2</sup> in units of  $e/2m_N^3$ . Sector contributions are for a single quark having unit charge. The fit windows are selected using the criteria outlined in Ref. [14].

$m_\pi^2$ (GeV <sup>2</sup> )	$u_\Delta$			$d_\Delta$		
	fit value	fit window	$\chi_{\text{dof}}^2$	fit value	fit window	$\chi_{\text{dof}}^2$
0.9972(55)	0.19(58)	18 – 22	0.83	0.19(58)	18 – 22	0.83
0.8936(56)	0.19(68)	18 – 22	0.63	0.19(68)	18 – 22	0.63
0.7920(55)	0.18(82)	18 – 22	0.50	0.18(82)	18 – 22	0.50
0.6920(54)	0.2(1.0)	18 – 22	0.44	0.2(1.0)	18 – 22	0.44
0.6910(35)	−0.10(75)	18 – 22	0.74	−0.10(75)	18 – 22	0.74
0.5925(33)	−0.09(87)	18 – 20	1.01	−0.09(87)	18 – 20	1.01
0.4854(31)	−0.2(1.2)	18 – 20	0.92	−0.2(1.2)	18 – 20	0.92
0.3795(31)	−0.4(1.4)	16 – 18	0.44	−0.4(1.4)	16 – 18	0.44
0.2839(33)	−0.8(1.6)	15 – 17	0.01	−0.8(1.6)	15 – 17	0.01
0.2153(35)	−1.2(1.9)	15 – 17	0.12	−1.2(1.9)	15 – 17	0.12
0.1384(43)	−2.4(2.5)	15 – 17	0.37	−2.4(2.5)	15 – 17	0.37
0.0939(44)	−3.7(3.3)	15 – 17	0.32	−3.7(3.3)	15 – 17	0.32

TABLE XXI: Quark sector contributions to the  $M3$  form factor of  $\Sigma^*$  baryons at  $Q^2 = 0.230(1)$  GeV<sup>2</sup> in units of  $e/2m_N^3$ . Sector contributions are for a single quark having unit charge. The fit windows are selected using the criteria outlined in Ref. [14].

$m_\pi^2$ (GeV <sup>2</sup> )	$u_{\Sigma^*}$ or $d_{\Sigma^*}$			$s_{\Sigma^*}$		
	fit value	fit window	$\chi_{\text{dof}}^2$	fit value	fit window	$\chi_{\text{dof}}^2$
0.9972(55)	0.13(81)	18 – 22	0.56	0.64(80)	18 – 22	0.50
0.8936(56)	0.12(91)	18 – 22	0.50	0.63(90)	18 – 22	0.44
0.7920(55)	0.1(1.0)	18 – 22	0.48	0.6(1.0)	18 – 22	0.39
0.6920(54)	0.1(1.2)	18 – 22	0.47	0.6(1.2)	18 – 22	0.38
0.6910(35)	−0.16(89)	18 – 22	0.96	0.10(89)	18 – 22	0.64
0.5925(33)	−0.1(1.0)	18 – 20	1.03	−0.1(1.0)	18 – 20	0.90
0.4854(31)	−0.2(1.2)	18 – 20	0.92	−0.2(1.2)	18 – 20	0.92
0.3795(31)	−0.3(1.3)	16 – 18	0.43	−0.3(1.3)	16 – 18	0.61
0.2839(33)	−0.5(1.4)	15 – 17	0.01	−0.4(1.4)	15 – 17	0.30
0.2153(35)	−0.7(1.6)	15 – 17	0.01	−0.5(1.5)	15 – 17	0.38
0.1384(43)	−1.1(1.8)	15 – 17	0.21	−0.8(1.7)	15 – 17	0.07
0.0939(44)	−1.2(2.0)	15 – 17	0.07	−1.1(2.0)	15 – 17	0.89



TABLE XXII: Quark sector contributions to the  $M3$  form factor of  $\Xi^*$  baryons at  $Q^2 = 0.230(1)$  GeV<sup>2</sup> in units of  $e/2m_N^3$ . Sector contributions are for a single quark having unit charge. The fit windows are selected using the criteria outlined in Ref. [14].

$m_\pi^2$ (GeV <sup>2</sup> )	$s_{\Xi^*}$			$u_{\Xi^*}$ or $d_{\Xi^*}$		
	fit value	fit window	$\chi_{\text{dof}}^2$	fit value	fit window	$\chi_{\text{dof}}^2$
0.9972(55)	0.6(1.1)	18 – 22	0.39	−0.1(1.2)	18 – 22	0.45
0.8936(56)	0.6(1.2)	18 – 22	0.39	−0.1(1.2)	18 – 22	0.48
0.7920(55)	0.5(1.3)	18 – 22	0.40	−0.1(1.3)	18 – 22	0.52
0.6920(54)	0.5(1.4)	18 – 22	0.41	0.0(1.4)	18 – 22	0.53
0.6910(35)	−0.2(1.1)	18 – 22	0.83	−0.3(1.1)	18 – 22	1.27
0.5925(33)	−0.2(1.1)	18 – 20	0.92	−0.2(1.1)	18 – 20	1.03
0.4854(31)	−0.2(1.2)	18 – 20	0.92	−0.2(1.2)	18 – 20	0.92
0.3795(31)	−0.3(1.2)	16 – 18	0.62	−0.3(1.2)	16 – 18	0.54
0.2839(33)	−0.3(1.3)	15 – 17	0.52	−0.4(1.3)	15 – 17	0.17
0.2153(35)	−0.3(1.3)	15 – 17	0.63	−0.4(1.4)	15 – 17	0.05
0.1384(43)	−0.3(1.4)	15 – 17	0.23	−0.6(1.4)	15 – 17	0.47
0.0939(44)	−0.4(1.4)	15 – 17	0.44	−0.3(1.5)	15 – 17	0.82

TABLE XXIII:  $M3$  form factor results at  $Q^2 = 0.230(1)$  GeV<sup>2</sup> of the charged decuplet baryons in units of  $e/2m_N^3$  for different  $m_\pi^2$  values. The  $M3$  form factor of the  $\Delta^-$  at the  $SU(3)_{\text{flavor}}$  limit where  $m_\pi^2 = 0.485(3)$  provides the  $M3$  form factor of  $\Omega^-$ .

$m_\pi^2$ (GeV <sup>2</sup> )	$\Delta^{++}$	$\Delta^+$	$\Delta^-$	$\Sigma^{*+}$	$\Sigma^{*-}$	$\Xi^{*-}$
0.9972(55)	0.4(1.2)	0.19(58)	−0.19(58)	−0.04(86)	−0.30(79)	−0.4(1.1)
0.8936(56)	0.4(1.4)	0.19(68)	−0.19(68)	−0.05(94)	−0.29(89)	−0.4(1.2)
0.7920(55)	0.4(1.6)	0.18(82)	−0.18(82)	−0.1(1.1)	−0.3(1.0)	−0.3(1.3)
0.6920(54)	0.4(2.0)	0.2(1.0)	−0.2(1.0)	−0.1(1.2)	−0.3(1.2)	−0.3(1.4)
0.6910(35)	−0.2(1.5)	−0.10(75)	0.10(75)	−0.18(90)	0.14(88)	0.2(1.1)
0.5925(33)	−0.2(1.7)	−0.09(87)	0.09(87)	−0.2(1.0)	0.1(1.0)	0.2(1.1)
0.4854(31)	−0.5(2.4)	−0.2(1.2)	0.2(1.2)	−0.2(1.2)	0.2(1.2)	0.2(1.2)
0.3795(31)	−0.8(2.8)	−0.4(1.4)	0.4(1.4)	−0.3(1.3)	0.3(1.3)	0.3(1.2)
0.2839(33)	−1.6(3.1)	−0.8(1.6)	0.8(1.6)	−0.6(1.4)	0.5(1.4)	0.3(1.3)
0.2153(35)	−2.4(3.8)	−1.2(1.9)	1.2(1.9)	−0.7(1.6)	0.6(1.5)	0.3(1.3)
0.1384(43)	−4.9(4.9)	−2.4(2.5)	2.4(2.5)	−1.2(1.9)	1.0(1.7)	0.4(1.4)
0.0939(44)	−7.4(6.6)	−3.7(3.3)	3.7(3.3)	−1.3(2.2)	1.2(1.9)	0.4(1.4)

TABLE XXIV: Collected results for the  $\Omega^-$ . Results are obtained from the  $\Delta^-$  at the  $SU(3)_{\text{flavor}}$  limit, where  $m_\pi^2 = 0.4854(31)$  GeV<sup>2</sup>.

quantity	fit value
mass (GeV)	1.732(12)
charge radius (fm <sup>2</sup> )	−0.307(15)
magnetic moment ( $\mu_N$ )	−1.697(65)
$E2$ form factor ( $10^{-2}\text{fm}^2$ )	0.86(12)
$M3$ form factor ( $e/2m_N^3$ )	0.2(1.2)

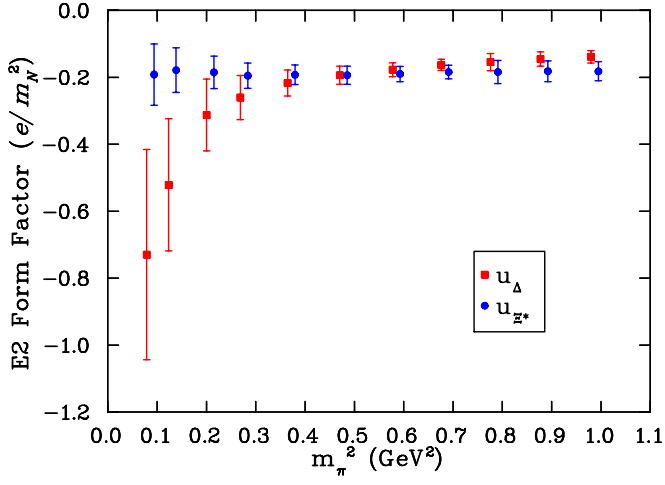


FIG. 29:  $E2$  form factor contributions from the  $u$  quark sectors of the  $\Delta$  and  $\Xi^*$ .

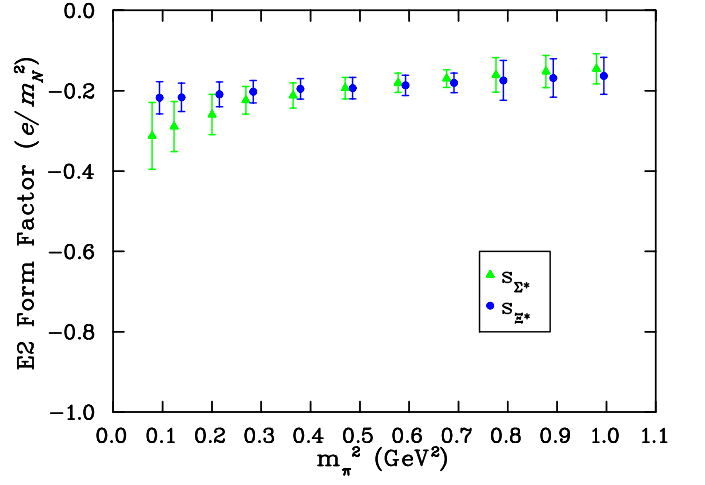


FIG. 31:  $E2$  form factor contributions from the  $s$  quark sectors of the  $\Sigma^*$  and  $\Xi^*$ .

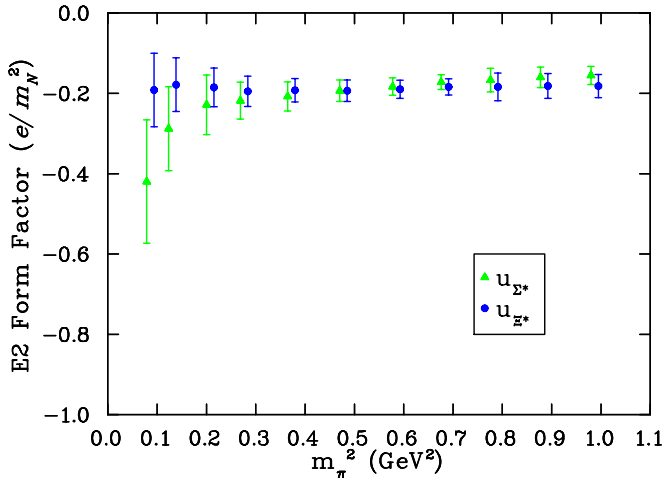


FIG. 30:  $E2$  form factor contributions from the  $u$  quark sectors of the  $\Sigma^*$  and  $\Xi^*$ .

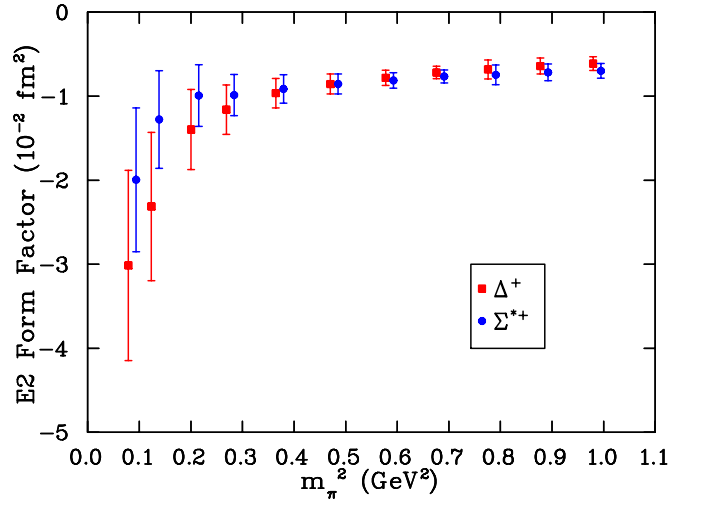


FIG. 32: Values of the  $E2$  form factors in units of  $10^{-2} \text{fm}^2$  for the  $\Delta^+$  and  $\Sigma^{*+}$  at different quark masses. The values for  $\Delta^+$  are plotted at shifted  $m_\pi^2$  for clarity.

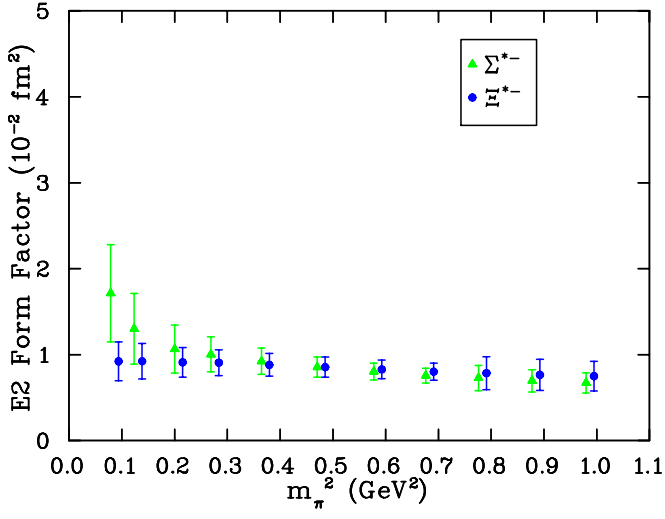


FIG. 33:  $E2$  form factors in units of  $10^{-2}\text{fm}^2$  for the  $\Sigma^{*-}$  and  $\Xi^{*-}$  at different quark masses. The values for  $\Sigma^{*-}$  are plotted at shifted  $m_\pi^2$  for clarity.

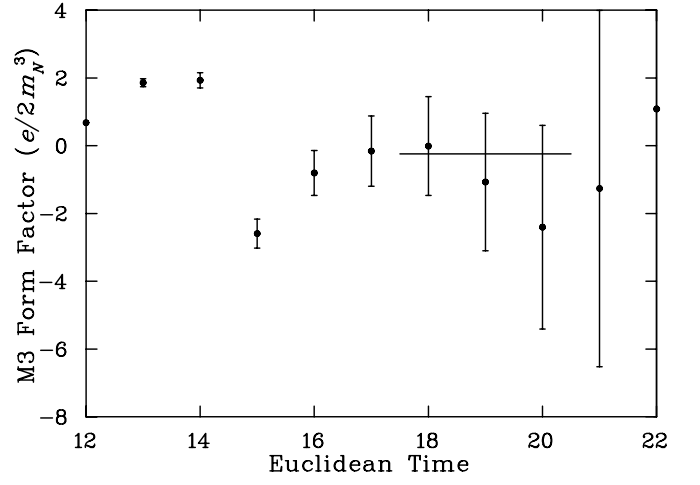


FIG. 35:  $M3$  form factor of the  $\Delta$  at the  $SU(3)_{\text{flavor}}$  limit as a function of time.

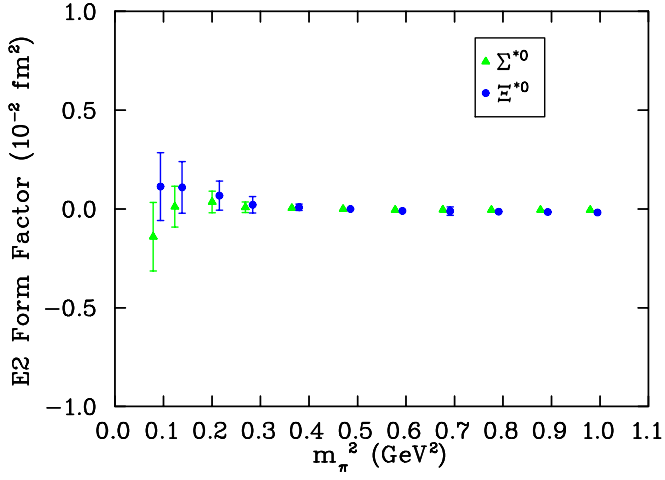


FIG. 34:  $E2$  form factors in units of  $10^{-2}\text{fm}^2$  for the  $\Sigma^{*0}$  and  $\Xi^{*0}$  at different quark masses. The values for  $\Sigma^{*0}$  are plotted at shifted  $m_\pi^2$  for clarity.

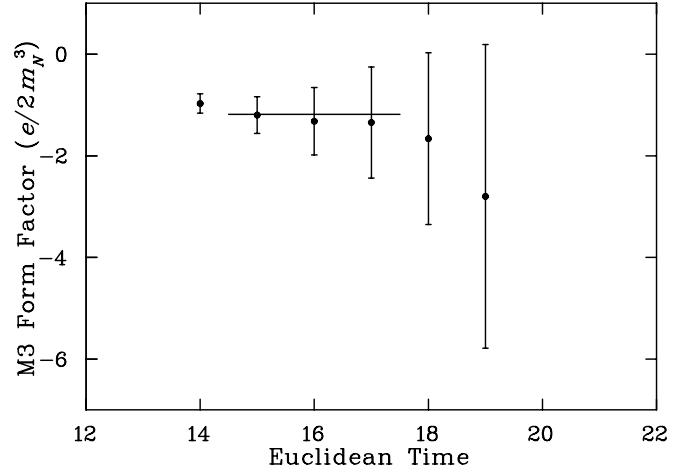


FIG. 36:  $M3$  form factor (splitting) of the  $u$  quark sector of the  $\Delta$  at the ninth quark mass where  $m_\pi^2 = 0.215(4)\text{GeV}^2$  as a function of time.

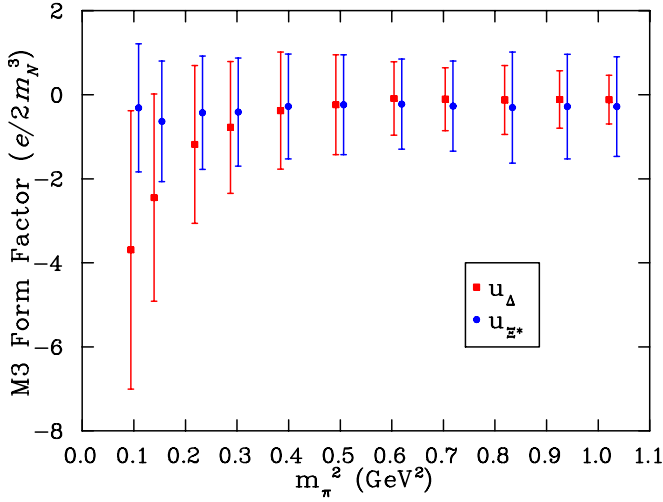


FIG. 37:  $M3$  form factor contributions from the  $u$  quark sectors of the  $\Delta$  and  $\Sigma^*$ . The results for the  $\Sigma^*$  are offset for clarity.

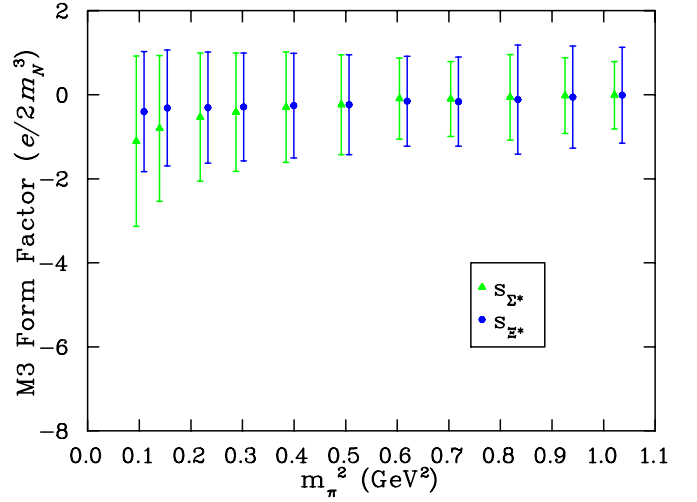


FIG. 39:  $M3$  form factor contributions from the  $s$  quark sectors of the  $\Sigma^*$  and  $\Xi^*$ . The results for the  $\Xi^*$  have been offset for clarity.

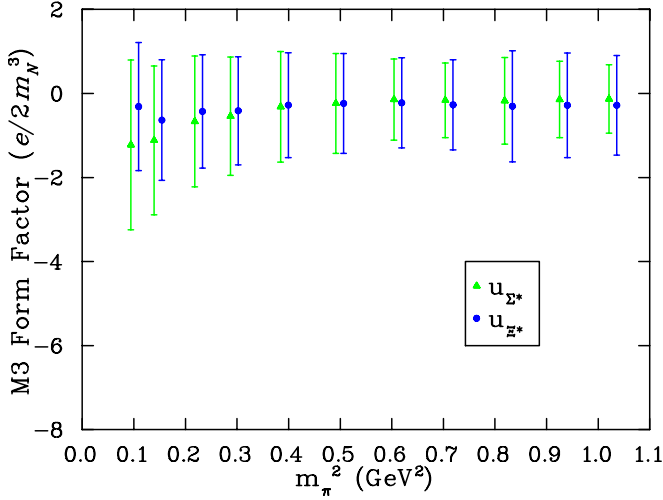


FIG. 38:  $M3$  form factor contributions from the  $u$  quark sectors of the  $\Sigma^*$  and  $\Xi^*$ . The results for the  $\Xi^*$  have been offset for clarity.

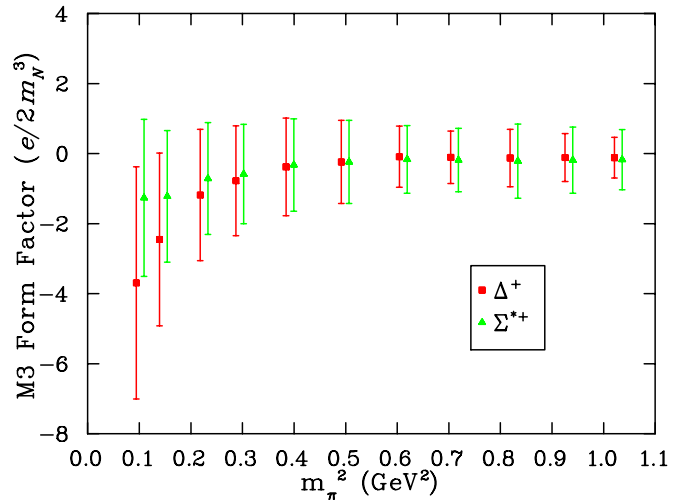


FIG. 40:  $M3$  form factors for the  $\Delta^+$  and  $\Sigma^{*+}$  at different quark masses. The values for  $\Sigma^{*+}$  are plotted at shifted  $m_\pi^2$  for clarity.

## VI. SUMMARY

We have performed an extensive calculation of the electromagnetic properties of decuplet baryons at both the quark level and the baryon level, including the quadrupole and octupole form factors of the spin-3/2 baryons. For the first time we obtain non-trivial results for both the  $E2$  and  $M3$  form factors. In particular, we find decuplet baryons to be oblate in shape.

We find that the quarks in the decuplet are not as sensitive to their environment as their octet counterparts. Of particular note, is the discovery that the decuplet-baryon radii are *smaller* than that of the octet baryons,

contradicting the simple quark model, but substantiating hints in the early study of Ref. [7].

A particularly interesting finding is that the suppression of sea-quark loop contributions in QQCD reduces the decuplet magnetic moment considerably, resulting in a turnover in the magnetic moment at light quark masses, as illustrated in Fig. 25. At large pion masses, the  $\Delta^+$  moment is enhanced relative to the proton moment in accord with earlier quenched lattice QCD calculations [7, 23] and model expectations. However, as the chiral regime is approached, the non-analytic behavior of the quenched meson cloud is revealed, enhancing the proton and suppressing the  $\Delta^+$ , in accord with the expectations

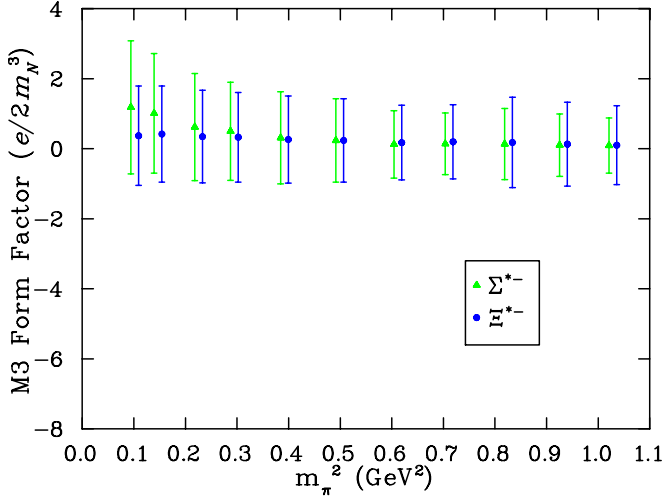


FIG. 41:  $M3$  form factors for the  $\Sigma^{*-}$  and  $\Xi^{*-}$  at different quark masses. The values for  $\Xi^{*-}$  are plotted at shifted  $m_\pi^2$  for clarity.

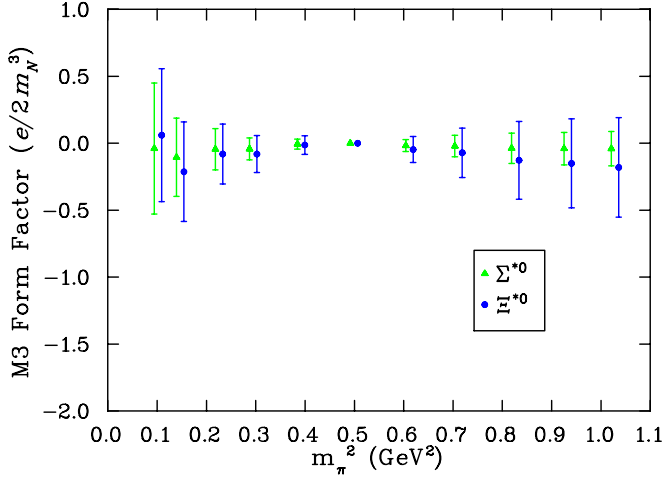


FIG. 42:  $M3$  form factors for the  $\Sigma^{*0}$  and  $\Xi^{*0}$  at different quark masses. The values for  $\Xi^{*0}$  are plotted at shifted  $m_\pi^2$  for clarity.

of  $Q\chi$ PT. This suppression should be absent in full QCD. Hence this is one particular case that we have identified as a place to look for effects of unquenching in future dynamical simulations. We also predict that unquenching effects should be observed in the  $\Omega^-$  magnetic moment, which we find to be suppressed in quenched QCD with regard to the experimentally measured value due to the absence of  $K\Xi$  loops in the virtual decay of  $\Omega^-$ .

Through a calculation of the decuplet E2 form factors and electric quadrupole moments, we predict oblate shapes for the decuplet baryons. It will be interesting to confront this prediction with an experimental measurement of the  $\Omega^-$  quadrupole form factor. We provide a summary of all the  $\Omega^-$  measurements in Table XXIV.

Finally we have obtained non-trivial values for the  $M3$  form factor for the first time in lattice QCD studies. These results provide an interesting and novel forum for the further development of our understanding of non-perturbative QCD.

## Acknowledgments

We thank the Australian Partnership for Advanced Computing (APAC) and the South Australian Partnership for Advanced Computing (SAPAC) for generous grants of supercomputer time which have enabled this project. This work was supported by the Australian Research Council. J.Z. is supported by STFC grant PP/F009658/1. JBZ is supported by Chinese NSFC-Grant No. 10675101 and 10835002.

- 
- [1] J. Arrington, C. D. Roberts and J. M. Zanotti, arXiv:nucl-th/0611050.
  - [2] K. de Jager, arXiv:nucl-ex/0612026.
  - [3] H. y. Gao, Int. J. Mod. Phys. E **12**, 1 (2003) [Erratum-ibid. E **12**, 567 (2003)] [arXiv:nucl-ex/0301002].
  - [4] C. E. Hyde-Wright and K. de Jager, Ann. Rev. Nucl. Part. Sci. **54**, 217 (2004) [arXiv:nucl-ex/0507001].
  - [5] C. F. Perdrisat, V. Punjabi and M. Vanderhaeghen, arXiv:hep-ph/0612014.
  - [6] J. M. Zanotti, PoS **LATTICE2008**, 007 (2008) [arXiv:0812.3845 [hep-lat]].
  - [7] D. B. Leinweber, T. Draper and R. M. Woloshyn, Phys. Rev. D **46**, 3067 (1992) [arXiv:hep-lat/9208025].
  - [8] C. Alexandrou, T. Korzec, T. Leontiou, J. W. Negele and A. Tsapalis, PoS **LATTICE2007**, 149 (2007) [arXiv:0710.2744 [hep-lat]].
  - [9] C. Alexandrou *et al.*, arXiv:0810.3976 [hep-lat].
  - [10] D. B. Leinweber *et al.*, Phys. Rev. Lett. **94**, 212001 (2005) [arXiv:hep-lat/0406002].
  - [11] D. B. Leinweber *et al.*, Phys. Rev. Lett. **97**, 022001 (2006) [arXiv:hep-lat/0601025].
  - [12] R. D. Young, J. Roche, R. D. Carlini and A. W. Thomas, Phys. Rev. Lett. **97**, 102002 (2006) [arXiv:nucl-ex/0604010].
  - [13] A. Acha *et al.* [HAPPEX collaboration], Phys. Rev. Lett. **98**, 032301 (2007) [arXiv:nucl-ex/0609002].

- [14] S. Boinepalli, D. B. Leinweber, A. G. Williams, J. M. Zanotti and J. B. Zhang, Phys. Rev. D **74**, 093005 (2006) [arXiv:hep-lat/0604022].
- [15] J. N. Hedditch, W. Kamleh, B. G. Lasscock, D. B. Leinweber, A. G. Williams and J. M. Zanotti, arXiv:hep-lat/0703014.
- [16] B. L. Ioffe, Nucl. Phys. B **188**, 317 (1981) [Erratum-ibid. B **191**, 591 (1981)].
- [17] Y. Chung, H. G. Dosch, M. Kremer and D. Schall, Nucl. Phys. B **197**, 55 (1982).
- [18] J.J. Sakurai, "Advanced Quantum Mechanics" (Addison-Wesley, 1982).
- [19] Y. Kuramashi, M. Fukugita, H. Mino, M. Okawa and A. Ukawa, Phys. Rev. Lett. **71**, 2387 (1993).
- [20] S. J. Dong and K. F. Liu, Phys. Lett. B **328**, 130 (1994) [arXiv:hep-lat/9308015].
- [21] M. Benmerrouche, R. M. Davidson and N. C. Mukhopadhyay, Phys. Rev. C **39**, 2339 (1989).
- [22] S. Nozawa and D. B. Leinweber, Phys. Rev. D **42**, 3567 (1990).
- [23] D. B. Leinweber, R. M. Woloshyn and T. Draper, Phys. Rev. D **43**, 1659 (1991).
- [24] W. Wilcox, T. Draper and K. F. Liu, Phys. Rev. D **46**, 1109 (1992) [arXiv:hep-lat/9205015].
- [25] M. Luscher and P. Weisz, Commun. Math. Phys. **97**, 59 (1985) [ibid. **98**, 433 (1985)].
- [26] R. Sommer, Nucl. Phys. B **411**, 839 (1994) [arXiv:hep-lat/9310022].
- [27] J. M. Zanotti *et al.* [CSSM Lattice Collaboration], Phys. Rev. D **65**, 074507 (2002) [arXiv:hep-lat/0110216].
- [28] J. M. Zanotti, B. Lasscock, D. B. Leinweber and A. G. Williams, Phys. Rev. D **71**, 034510 (2005) [arXiv:hep-lat/0405015].
- [29] S. Boinepalli, W. Kamleh, D. B. Leinweber, A. G. Williams and J. M. Zanotti, Phys. Lett. B **616**, 196 (2005) [arXiv:hep-lat/0405026].
- [30] W. Kamleh, D. B. Leinweber and A. G. Williams, Phys. Rev. D **70**, 014502 (2004) [arXiv:hep-lat/0403019].
- [31] R. D. Young, D. B. Leinweber, A. W. Thomas and S. W. Wright, Phys. Rev. D **66**, 094507 (2002) [arXiv:hep-lat/0205017].
- [32] J. N. Labrenz and S. R. Sharpe, Phys. Rev. D **54**, 4595 (1996) [arXiv:hep-lat/9605034].
- [33] D. B. Leinweber *et al.*, [arXiv:nucl-th/02111014].
- [34] M. Gockeler *et al.*, [QCDSF Collaboration], Phys. Rev. D **71**, 034508 (2005) [arXiv:hep-lat/0303019].
- [35] D. B. Leinweber, Phys. Rev. D **47**, 5096 (1993) [arXiv:hep-ph/9302266].
- [36] I. C. Cloet, D. B. Leinweber and A. W. Thomas, Phys. Lett. B **563**, 157 (2003) [arXiv:hep-lat/0302008].
- [37] D. B. Leinweber, A. W. Thomas, A. G. Williams, R. D. Young, J. M. Zanotti and J. B. Zhang, Nucl. Phys. A **737**, 177 (2004) [arXiv:nucl-th/0308083].